이학박사 학위논문

Single Electron Tunneling Spectroscopic Study on Vortices in Cuprate Superconductors

단전자 터널링 스펙트로스코피를 이용한 구리 산화물 계열 초전도체의 볼텍스에 관한 연구

2023년 2월

서울대학교 대학원

물리천문학부

박 민 석

Single Electron Tunneling Spectroscopic Study on Vortices in Cuprate Superconductors

지도 교수 이 진 호

이 논문을 이학박사 학위논문으로 제출함

2023년 1월

서울대학교 대학원

물리천문학부

박 민 석

박민석의 이학박사 학위논문을 인준함

2023년 1월

위 원 장 _____ 민 홍 기 _____ (인)

부위원장 _____ 이 진 호 _____ (인)

위 원 _____ 최 석 봉 _____ (인)

위 원 _____ 장 준 호 _____ (인)

위 원 _____ 정 창 욱 _____ (인)

Abstract

After the discovery of high-temperature superconductors in 1986, many researchers around the world have made numerous efforts to explain the phenomena. Especially, STM has played a leading role in improving the understanding of high-temperature superconductivity. Even now, numerous STM results are being published annually by various groups worldwide.

In general, the measurement of the superconductor using STM is performed at the liquid helium boiling temperature. However, a dilution refrigerator (DR) provides an extremely low-temperature environment for the measurements. The DR is a very delicate and complex equipment that is particularly difficult to handle, and the vibration is easily induced during its operation. On the other hand, STM is very sensitive to vibration, so combining them is a very difficult task. Nevertheless, we overcame these difficulties and realized the DR-STM successfully.

Additionally, using this DR-STM, we investigated superconducting vortices using a special Coulomb blockade tip, which is very charge sensitive, and we were able to measure the vortex charge distribution. Our result is the first direct observation of the vortex charges with a spatial resolution, and it shows that the electron density tends to be lower in vortices than in the non-vortex regions.

Keywords: Scanning Tunneling Microscopy, Dilution Refrigerator, High-T_c superconductor, Single Electron Tunneling, Vortex Charge
Student Number: 2013-30115

Table of Contents

List of Figures and Tables

Chapter 1.

Spectroscopic Imaging Scanning Tunneling Microscopy

A scanning tunneling microscope (STM) is a microscope that measures surface structure of the sample in atomic resolution. It was invented by Gerd Binning and Heinrich Rohrer at IBM in 1981 [1], who are laureates of the Nobel Prize in Physics in 1986.

The STM has been widely used in the various fields of science and technology, especially in nanoscience. It measures sample surfaces in atomic scale and provides electronic structures in real space. Its resolution is usually $< 1\,\text{Å}$ in the $xy-$plane and $< 0.1\,\text{Å}$ in the $z-$direction. It is on the concept of the quantum tunneling effect, which happens when the tip is sufficiently close to the sample and a bias voltage is applied between them.

During STM measurement, the usual tip−sample distance is within a few Å, the usual sample bias voltages are in the range from a few $m\text{V}$ to a few V, and the resultant tunneling currents are in the range from a few $p\text{A}$ to a few $n\text{A}$. Since the tip−sample distance is too close, the stable conditions during the measurement are key factors for obtaining high−resolution STM images. This goal is achievable by reducing mechanical vibrations and electrical noises during measurements to an extremely low level.

1.1. Electron Tunneling

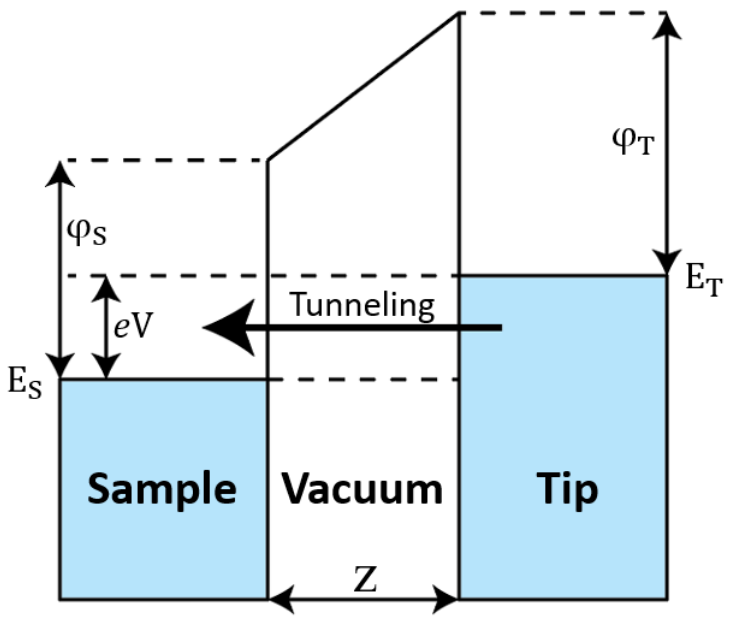

Figure 1.1: Schematic of the electron tunneling between tip and sample. This feature shows the energy diagram of the electron tunneling between tip and sample. A positive sample bias voltage lowers the energy on the sample side, then electron tunneling from the tip to the sample can happen.

In 1960, the electron tunneling between metal and superconductor was first realized by Ivar Giaever [2]. John Bardeen, an American physicist, tried to explain these phenomena using time−dependent perturbation theory [3]. According to his theory, the tunneling matrix element $M_{\mu\nu}$ is given by

$$M_{\mu\nu} = -\frac{\hbar^2}{2m}\oint dS\left(\psi_\mu \frac{\partial \psi_\nu}{\partial z} - \psi_\nu \frac{\partial \psi_\mu}{\partial z}\right) \tag{1.1}$$

for electron tunneling from μ state to ν state along $\hat{z}-$direction [4].

In these circumstances, a new microscope, which is called a STM, was invented by Gerd Binning and Heinrich Rohrer in 1981. A probe tip, which is installed on the piezo tube, is brought close to the sample within a few Å range, and the positive bias voltage is applied between them. As a result, electron tunneling from tip to sample happens. Under the elastic tunneling assumption, the Fermi−Golden rule determines the transfer rate of the electron from the sample to the tip.

$$w = \frac{2\pi}{\hbar}\left|M_{\mu\nu}\right|^2 \delta\left(E_\mu - E_\nu\right) \tag{1.2}$$

When a bias voltage V is applied to the sample at a finite temperature, the total tunneling current I is given by

$$\begin{aligned} I = \frac{4\pi e}{\hbar}\int_{-\infty}^{\infty} |M|^2 [f(E_F - eV + \varepsilon) - f(E_F + \varepsilon)] \\ \times \rho_T(E_F - eV + \varepsilon)\, \rho_S(E_F + \varepsilon)\, d\varepsilon \end{aligned} \tag{1.3}$$

, where $f(E)$ is the Fermi−Dirac distribution function,

$$f(E) = \frac{1}{1 + e^{(E - E_F)/k_B T}} \tag{1.4}$$

and ρ_T (ρ_S) is the density of states (DOS) of the tip (sample). At a sufficiently low temperature ($k_B T \ll 1$), the Fermi−Dirac distribution function can be approximated to a step function. As a result,

$$I = \frac{4\pi e}{\hbar}\int_0^{eV} |M|^2 \rho_T(E_F - eV + \varepsilon)\, \rho_S(E_F + \varepsilon)\, d\varepsilon \tag{1.5}$$

Assume that the tunneling matrix M does not vary appreciably [3].

According to Tersoff and Hamann' s calculation for an s−wave tip apex [5], the matrix element is given by

$$|M|^2 \propto \exp\left(-2\frac{\sqrt{2m\phi}}{\hbar}z\right) \tag{1.6}$$

, where m is the electron mass, ϕ is the work function and z is the tip−sample distance. Under the assumption that ρ_T is constant, the tunneling current is given by

$$I \propto \exp\left(-2\frac{\sqrt{2m\phi}}{\hbar}z\right)\rho_T\int_0^{eV}\rho_S(E_F+\varepsilon)d\varepsilon \tag{1.7}$$

In addition, the differential conductance of the tunneling current is given by

$$g(z,V) \equiv \frac{\mathrm{d}I}{\mathrm{d}V}(z,V) \propto \exp\left(-2\frac{\sqrt{2m\phi}}{\hbar}z\right)\rho_T\rho_S(eV) \tag{1.8}$$

, which shows that the differential conductance is proportional to the local density of states (LDOS) of the sample at fixed z and ϕ.

1.2. STM Measurement

The STM junction resistance is determined by setting the sample bias voltage and the set point current. If the tunneling current between tip and sample is smaller than the set point current, the piezoelectric tube stretches until the tunneling current reaches the

set point current, and vice versa. This is possible due to a proportional–integral–derivative (PID) controller, which employs feedback loop. A usual tunneling current is as low as tens of pA. These extremely small currents should be amplified by current preamplifier for the actual STM measurement.

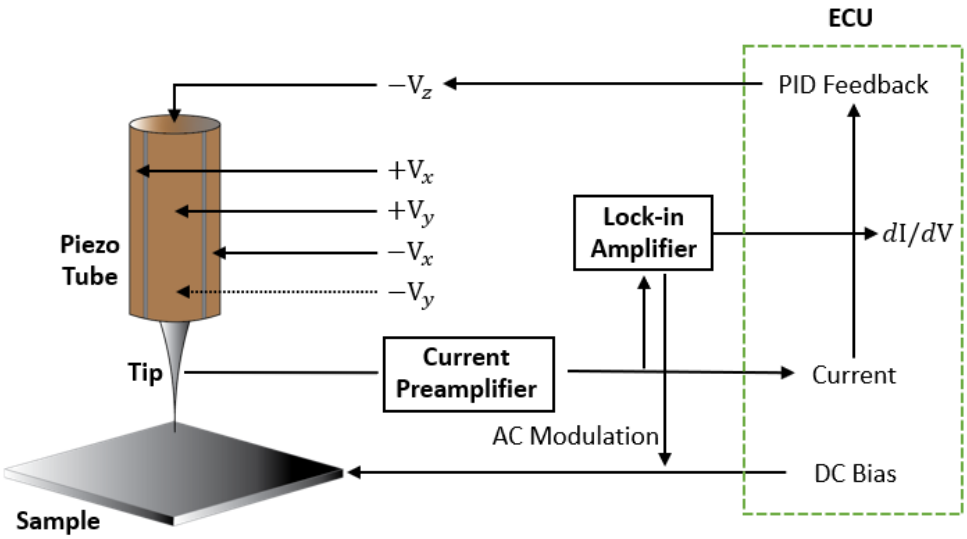

Figure 1.2: Schematic diagram of STM measurement.

1.3. Topography

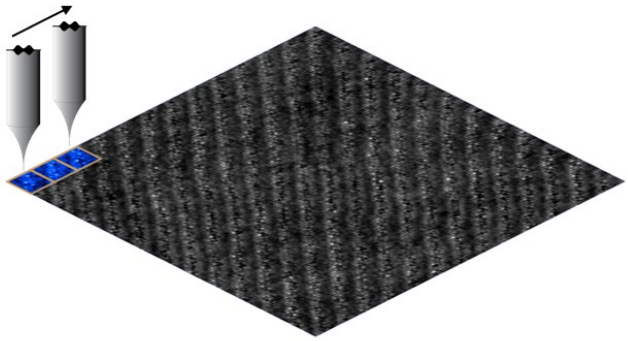

Figure 1.3: Schematic of topographic measurement.

In topographic measurement, there are two types of measurement modes. One is constant height mode, and the other is constant current mode. In constant height mode, which is simpler than the other, the voltage applied to the z−piezoelectric tube is constant, that is, the z value of the piezo tube is kept constant. In other words, the PID feedback loop is not working in this mode. Thus, the tip−sample distance varies at each position while scanning the sample. As a result, the tunneling current varies at each position. However, if the sample surface is too rough, there is a possibility of collision between the tip and the sample.

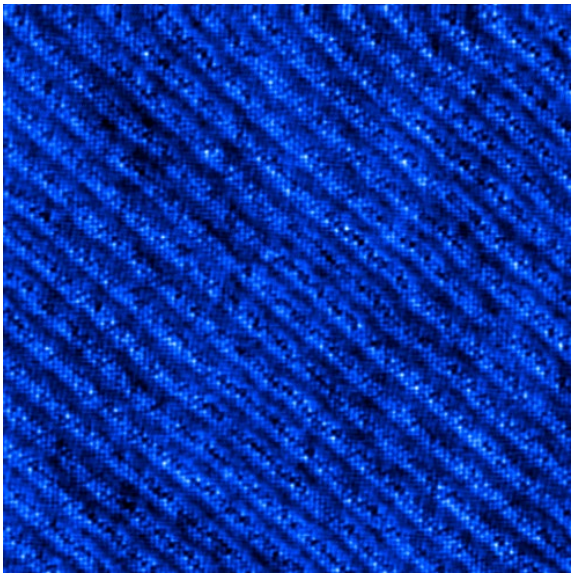

Figure 1.4: Topographic image of $\mathbf{Bi_2Sr_2CaCu_2O_{8+x}}$

Topographic image of $\mathrm{Bi_2Sr_2CaCu_2O_{8+x}}$ sample measured by tungsten tip at 4.2K using DR−STM ($50nm \times 50nm,\ V = 100mV,\ I = 80pA$).

In constant current mode, on the contrary, the tip height varies with the surface topography to keep the tunneling current constant by PID feedback loop. In this case, since the tunneling current is kept constant, the topography of a sample is measured by tip height at

each point while scanning. Figure 1.5 is the topographic image of $Bi_2Sr_2CaCu_2O_{8+x}$ measured by DR−STM.

1.4. Spectroscopy

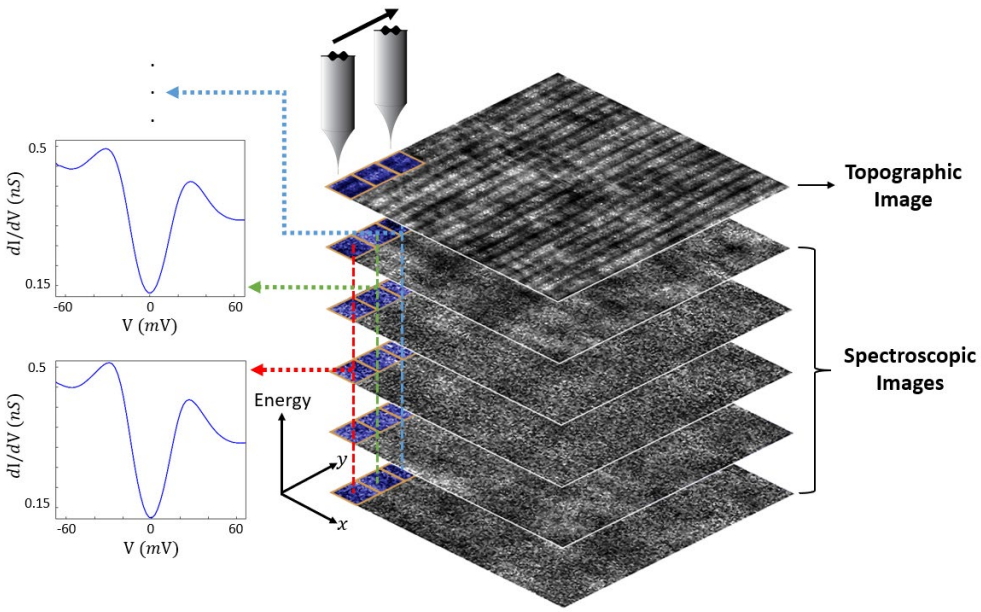

Figure 1.5: Schematic of spectroscopic measurement.

A virtual two−dimensional grid is assigned to the interesting region on the sample surface. The usual grid consists of tens of thousands of pixels. The tunneling current for the topographic image and the dI/dV for spectroscopic image are measured simultaneously at each pixel.

According to the equation 1.8, the differential conductance is proportional to the LDOS of a sample.

$$g(z,V) \equiv \frac{\mathrm{d}I}{\mathrm{d}V}(z,V) \propto \exp\left(-2\frac{\sqrt{2m\phi}}{\hbar}z\right)\rho_T\rho_S(eV) \qquad (1.9)$$

The differential conductance can be obtained in two different ways.

One is a direct mathematical differentiation of the tunneling current I with respect to sample bias voltage V. This is relatively simple method, but the result is usually too noisy. The other is using lock-in technique, which provides a better result compared to the previous method. We are going to use the Taylor series expansion of the tunneling current.

$$I(V) = I(V_0) + \frac{1}{1!}\frac{dI}{dV}\bigg|_{V=V_0}(V - V_0) + \frac{1}{2!}\frac{\mathrm{d}^2 I}{dV^2}\bigg|_{V=V_0}(V - V_0)^2 + \cdots$$

An AC modulation bias voltage $Asin(\omega t)$ is introduced to the DC sample bias voltage V_0. The Taylor expansion in this case is given by

$$\begin{aligned} I(V) &= I\big(V_0 + Asin(\omega t)\big) \\ &= I(V_0) + \frac{dI}{dV}\bigg|_{V=V_0} A\sin(\omega t) + \frac{1}{2}\frac{\mathrm{d}^2 I}{dV^2}\bigg|_{V=V_0} A^2\sin^2(\omega t) + \cdots \qquad (1.10) \end{aligned}$$

The result consists of DC term plus other harmonics. From the amplitude of the first harmonic signal, we can get the differential conductance. In the spectroscopic measurement, we assign a virtual two-dimensional lattice on the sample surface. The measurement of differential conductance at each point across a two-dimensional lattice gives a three-dimensional data structure. This measurement is especially called scanning tunneling spectroscopy. It takes a few days to complete the map so that the stability during measurement is the most important condition that we have to prepare. Furthermore, we have noted that the topographic image is also simultaneously measured during spectroscopic imaging.

1.5. STM Head

The DR-STM head consists of the scanner, the walker, the rotator, and the sample receptacle. The structure is based on the S. H. Pan's style [6].

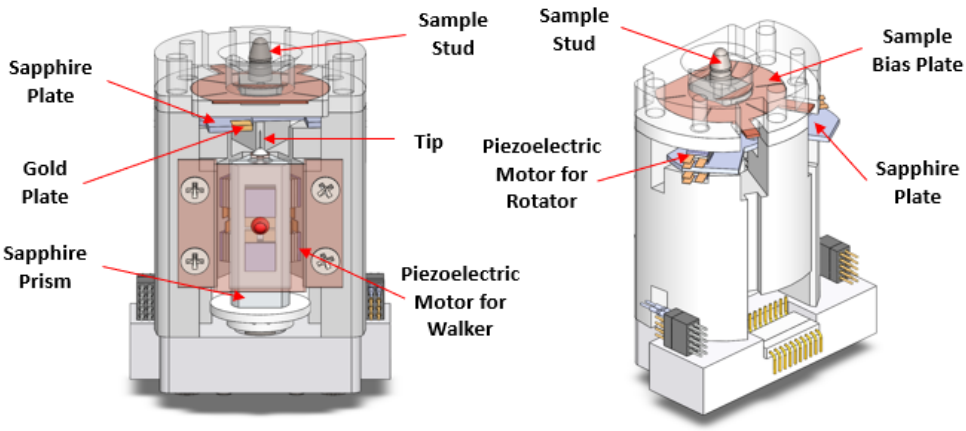

Figure 1.6: The 3D drawings of the DR-STM head.

A sample is attached to the surface of the sample stud. Then, it is loaded into the sample receptacle using a long transfer rod system. The sample stud is in contact with the sample bias plate, which is connected to the ECU and is used to give a bias voltage to the sample.

Meanwhile, the piezoelectric tube has five electrodes on the surface. Four of them control fine motions in $\pm x$ and $\pm y$ directions and they are on the outer surface. The other electrode for fine motion along z direction is on the inner surface. The piezoelectric tube is installed on the top of the scanner holder, which is made of MACOR ceramic. Then, the scanner holder is installed inside the triangular sapphire prism. This module is called a scanner. The scanner is in contact with

the two piezoelectric stacks at each triangular surface. The piezoelectric stacks are used for coarse movement of the scanner in z direction. This module is called a walker.

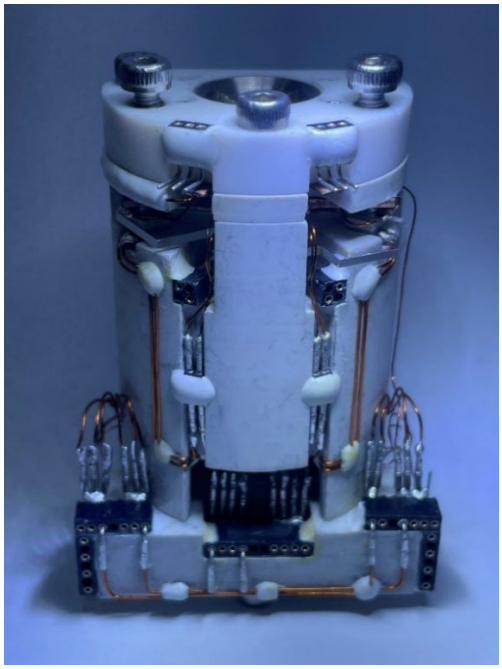

Figure 1.7: The DR-STM head.

The rotator is not included in the usual STM head design. It is a distinguished part of our group [7] and is used for tip treatment. The sharpness of the tip is crucial for STM measurement. If the tip is in poor condition, the resultant image is also poor. In that case, tip treatment is required. First, we need to replace the sample with the gold target for field emission, but it takes a day at least. It is very time-consuming, and the other problem is that the sample should be replaced.

To solve these problems, we installed a new tip treatment stage inside the head. The gold target is attached to the sapphire plate and

the plate can be rotated by four piezoelectric motors. This plate is installed between the tip and the sample. When the plate rotates in, the gold target is located above the tip and then field emission for tip treatment is ready. After finishing the tip treatment, the plate rotates out. This module is called a rotator. Using this module, we can save not only time but also the sample.

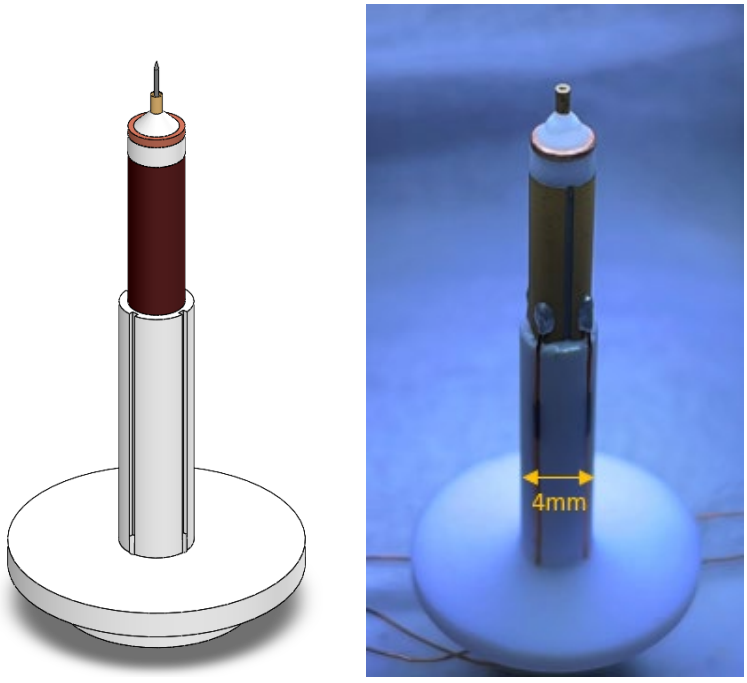

Figure 1.8: The scanner of STM head

The drawing of piezoelectric tube scanner with a tip installed (left), the real piezoelectric tube scanner for DR-STM (right).

Chapter 2.

SI-STM Laboratory

During STM measurement, the usual tip-sample distance is within a few Å. Furthermore, the spectroscopic measurement usually takes a few days to complete the map. Thus, stability during STM measurement is the most important condition that we have to prepare. Not only a low mechanical vibration but also a low electrical noise is required for this goal. We have realized a special laboratory for our STM measurement.

2.1. Ultra-Low Vibration Laboratory

The vibration isolation is the most important for STM measurement. To achieve this goal, we divide SI-STM laboratory into the control room, the ULV room, the pump room, and the sample preparation room.

All the vibration sources (e.g., mechanical pumps, a compressor, gas cylinders) are located in the pump room. The ULV room is isolated from other facilities by making the concrete container with a 20cm thick floor and 30cm thick wall and by inserting shock-absorbing materials between them. The pillars have been constructed using high-strength concrete inside the container and they provide four

independent STM measurement areas. In addition, 25 tons of high-density concrete block has been constructed on each pillar and it is isolated by six air springs. Furthermore, an acoustic room has been installed on each block to reduce the noise from outside. Inside the acoustic room, the STM frame has been installed and its legs are filled with tons of lead shots. A small air spring has been installed on the top of each leg. The hexa-plate, which is made of SUS to reduce magnetization, has been installed on the air springs, and the Dewar is attached under the hexa-plate.

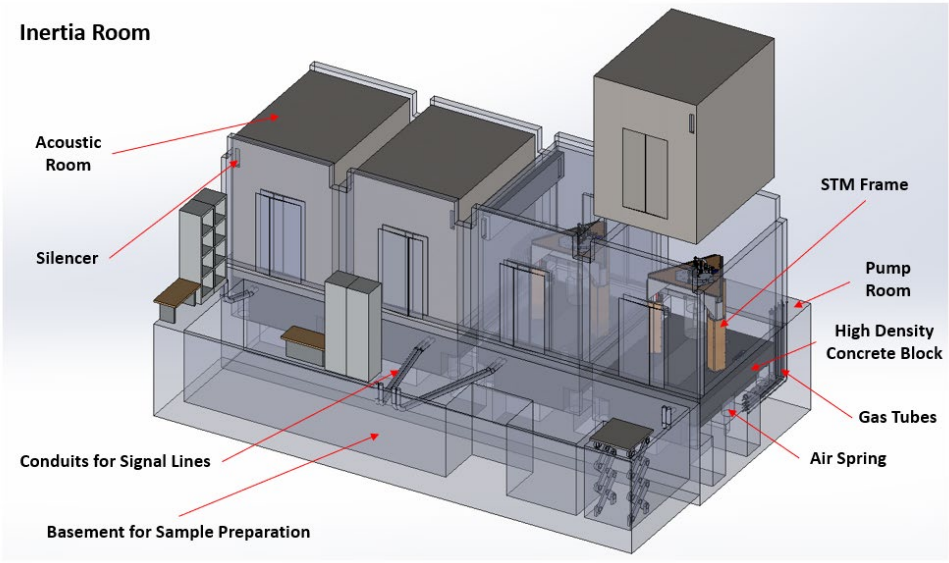

Figure 2.1: The 3D drawing of ultra-low vibration laboratory for STM measurement.

All the samples are prepared in the sample preparation room in the basement and the control of all the electronic devices for the STM measurement is conducted in the control room without entering the ULV room.

2.2. Gas Handling System (GHS)

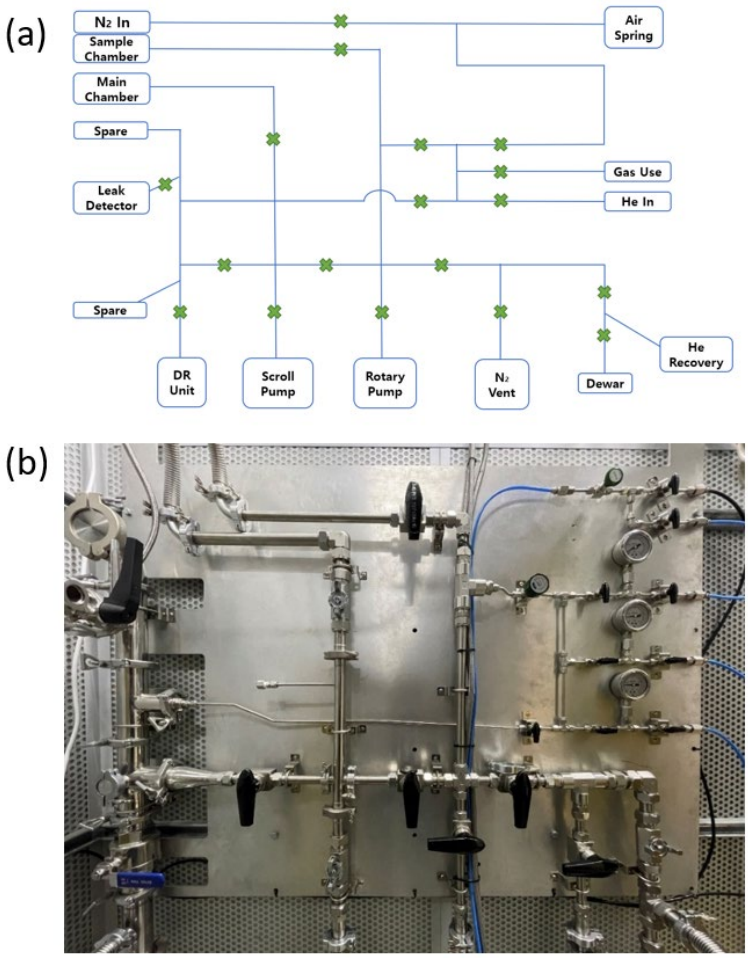

Figure 2.2: Gas handling system (GHS).

(a) Schematic diagram of GHS. (b) The realized GHS for DR−STM.

The gas handling system (GHS) has been installed inside the acoustic room. All the gas cylinders, mechanical pumps are located in the pump room, and they are connected to the acoustic room through the SUS tubes. It provides convenient handling for the pumping, flushing, or venting of the chamber. It is also very useful for the cooldown,

leak-check, air spring control, or liquid helium transfer. All the procedures for the preparation of STM measurement happen inside the acoustic room using this convenient GHS. Furthermore, we have a liquid He plant which collects He gas and liquefy the gas again. The experimental Dewar is directly connected to this plant.

2.3. Cryostat

Figure 2.3: The liquid helium Dewar for DR-STM.

The STM measurement is usually performed at liquid Helium (LHe) temperature, that is 4.2 K. Since the LHe evaporate continuously, the regular refilling is required to keep the temperature at 4.2 K.

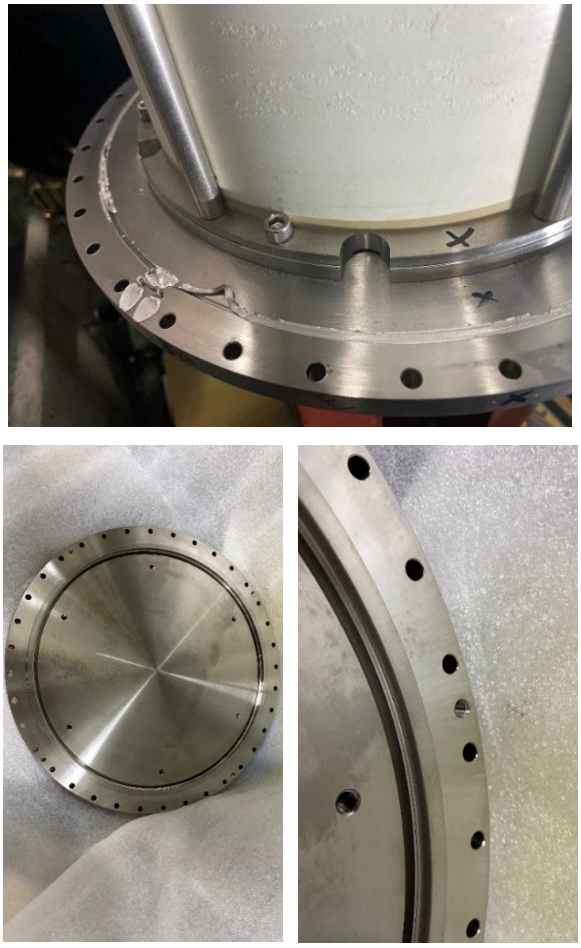

Figure 2.4: He bath flanges.

The previous He bath flange, which was very weak for He gas sealing (top), the improved He bath flange, which provides a better leak-tight ability with two stage barriers for blocking leakage (bottom).

However, frequent refilling causes a shorter period for STM measurement. To provide a longer lead time, thermal isolation is very important. This is achievable by a special storage container, which is called the Dewar which was invented by James Dewar in 1892. It is a vacuum-jacketed vessel, and the vacuum is a good thermal insulator. It is possible to preserve the cryogens (e.g., LN_2, LHe) for long periods. In other words, the evaporation rate of LHe is quite small and it guarantees a longer lead time for STM measurement.

There was a leakage on the He bath flange, so we made a new He bath flange, which consists of two-stage barriers for blocking leakage (Figure 2.4).

2.4. 14 Tesla Superconducting Magnet System

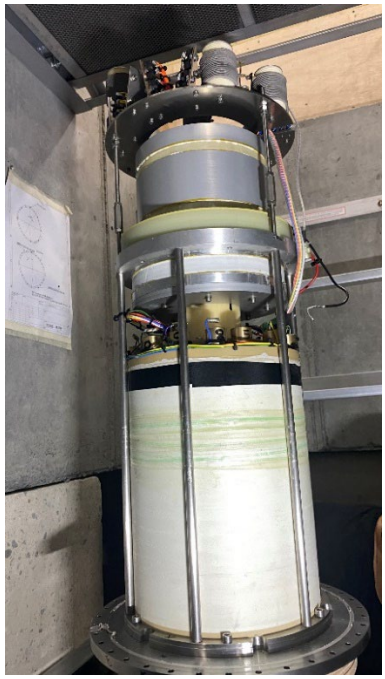

Figure 2.5: The real 14T superconducting magnet for DR-STM.

The superconducting magnet has been installed inside the He bath. If the He bath is filled with LHe, the magnet is also submerged into the LHe. A temperature sensor is on the top of the magnet, which shows the current magnet temperature. When we transfer LHe, we should check this temperature to adjust the LHe transfer rate. In addition, any thermal agitation from the magnet causes sudden LHe boiling off, which is called quenching. Also, the magnet can be damaged by

incorrect operation. Thus, we should operate the magnet very carefully.

The operation of 14 T superconducting magnet system consists of three steps: drive mode, persistent mode, and turning off persistent mode.

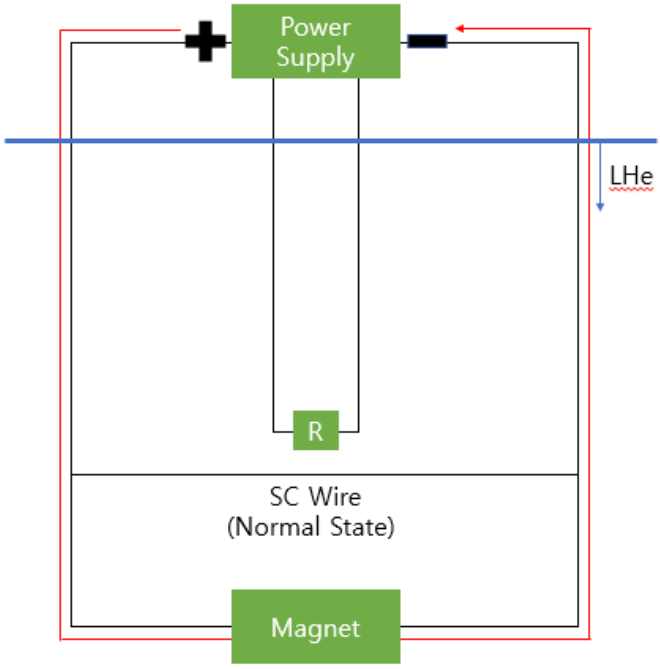

Figure 2.6: Drive mode.

Supply power to the magnet.

The superconducting magnet is below its critical temperature, so its wire is in the superconducting state. However, to give a current to the magnet, we need first to break its SC state by turning on the switch heater. Then the magnet wire turns into a normal metallic state. After, we can energize the magnet up to target tesla. This is called drive mode, and its schematic is in Fig.2.6. Then, the magnet automatically reaches the target tesla. In the persistent mode, we

need to break the connection of the magnet from the outer cable. After turning off the switch heater, the magnet turns into the superconducting state. Then, the dissipation of current in the magnet is zero.

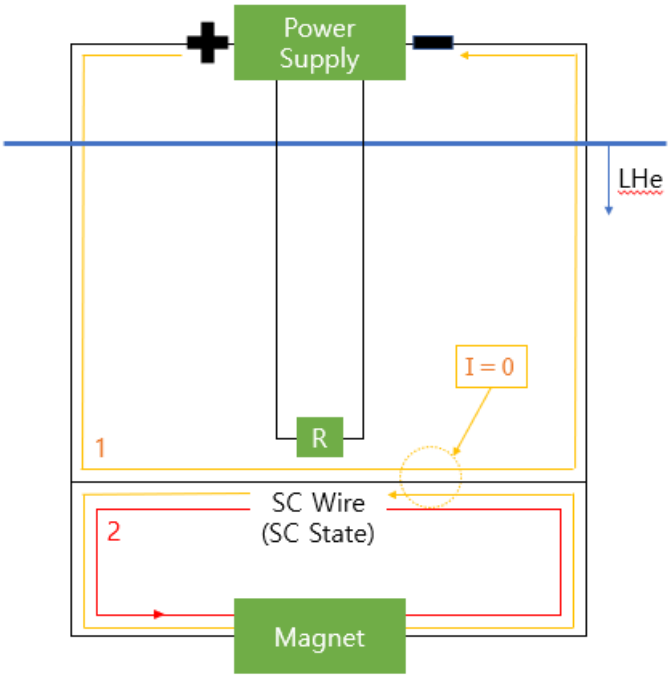

Figure 2.7: Persistent mode.

In this mode, the persistent current (2) is isolated from outside (1)

This is called the persistent mode in Fig.2.7. In this mode, we should lower the supplied current to zero. If we want to change the target tesla or turn off the magnet, we need to break the persistent mode. This is depicted in Fig.2.8. To do that, first we need to energize the magnet lead cable up to the previous current. Then, the switch heater should be turned on because the magnet should be connected to the power supply. After that, we need to adjust the current up to target tesla. After reaching target tesla, the switch heater should be turned off to break up the connection between the magnet and the power

supply.

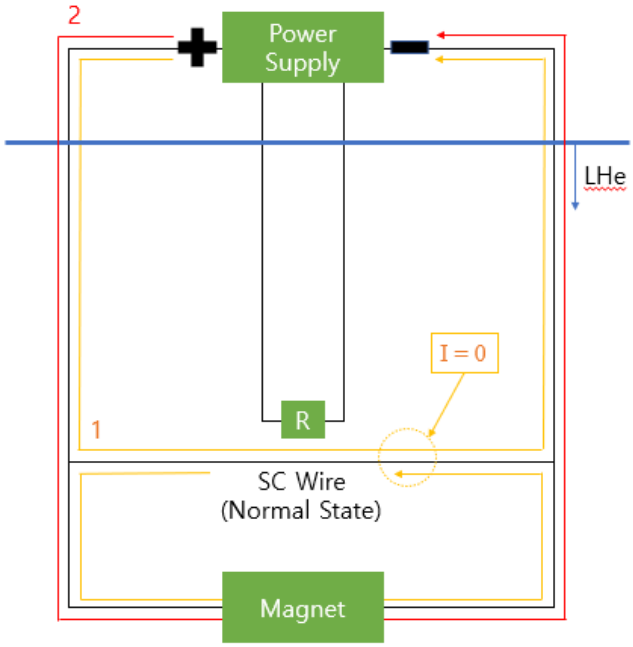

Figure 2.8: Turning off persistent mode.

2.5. Dilution Refrigerator

On 10 July 1908, Heike Kamerlingh Onnes at Leiden University first liquefied helium using the Joule–Thompson effect [8]. It was the greatest moment of low–temperature physics. After that, a number of subsequent low–temperature experiments were followed. Especially, during the measurement of the specific heat of liquid ^{4}He by Keesom and Clusius, a kink of specific heat at 2.17 K was found in 1932 [9]. This is the lambda point at which normal fluid helium turns into superfluid helium.

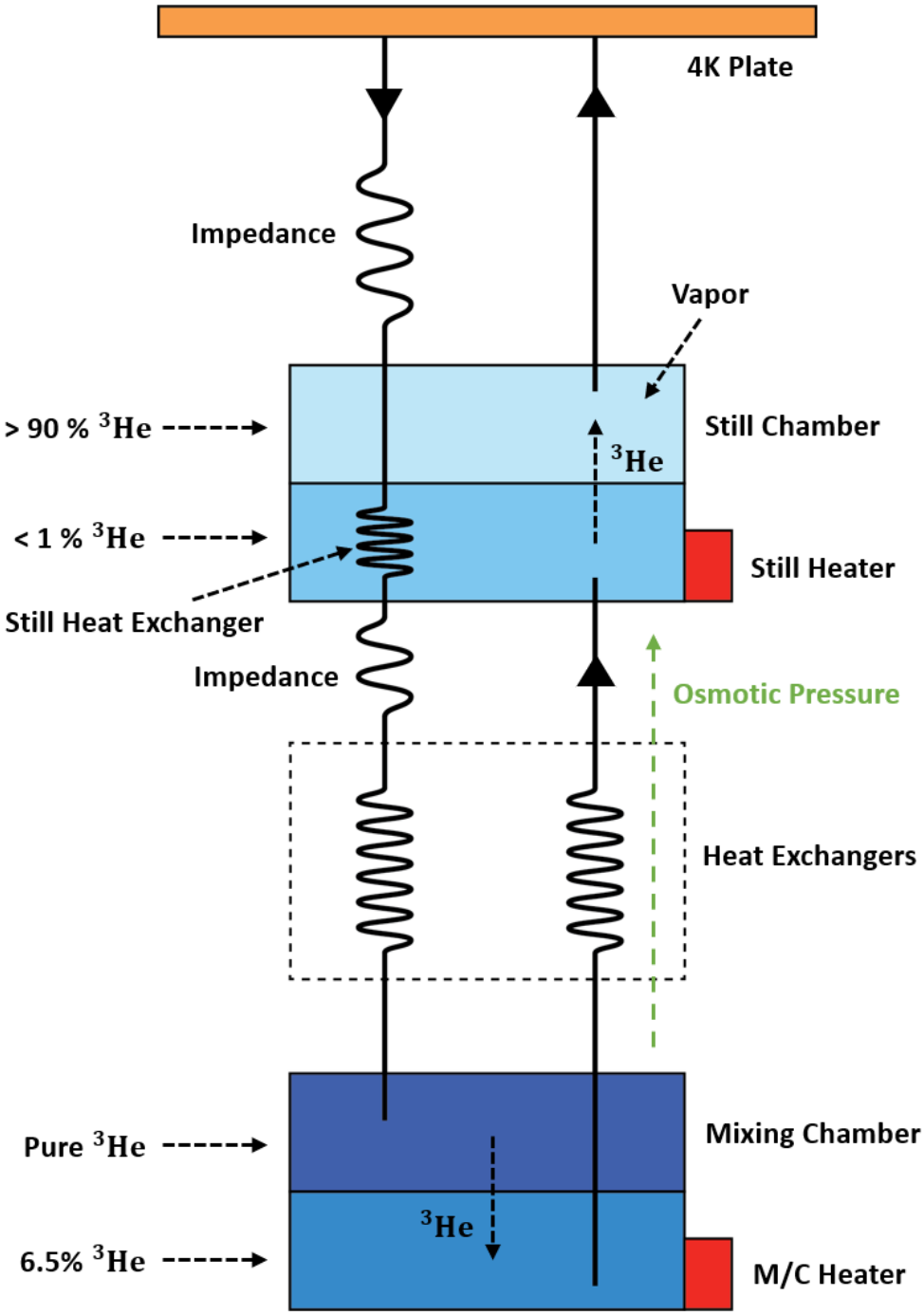

Figure 2.9: The schematic of dilution refrigerator.

In 1934, Mark Oliphant at the University of Cambridge first proposed the existence of ^{3}He [10]. In 1946, the idea on the separation of ^{3}He from ^{4}He was suggested by James Franck [11]. Soon after, the many subsequent experimental results on the separation of isotopes ^{3}He and ^{4}He were reported [12−14].

In 1951, a new cryogenic system using dilution of ^{3}He in superfluid ^{4}He was proposed by Heinz London at the Oxford conference on low−temperature physics. It was based on the idea regarding the quasiparticle behavior of diluted ^{3}He in superfluid ^{4}He, which was proposed by L. Landau and I. Pomeranchuk in 1948 [15]. In 1956, G. K. Walters and W. M. Fairbank discovered the phase separation of ^{3}He−^{4}He mixture into ^{3}He−rich phase and ^{3}He−poor phase below critical temperature 0.8 K using NMR techniques [16]. After that, London, Clarke, and Mendoza reported the essential experiments for dilution refrigeration in 1962 [17].

The DR unit consists of JT stage, still plate, cold plate, and mixing chamber. In 1964, this London−Clarke−Mendoza type refrigerator was finally realized at Leiden University [18]. The ^{3}He−rich liquid becomes pure ^{3}He liquid near zero temperature [19]. On the other hand, the ^{3}He concentration of ^{3}He−poor liquid is constant even near zero temperature [20]. The Clausius−Clapeyron relation is

$$\frac{dp}{d\mathrm{T}} = \frac{L}{\Delta V\, T} \tag{1.11}$$

Using the ideal gas law $pV = RT$, the vapor pressure is given by

$$p(T) = p_0 e^{-L/RT} \tag{1.12}$$

, where L is the latent heat. Since the latent heat of vaporization of ^{4}He is much higher than that of ^{3}He [21, 22], the vapor pressure of ^{3}He is much higher than that of ^{4}He. Thus, ^{3}He in the diluted phase preferentially evaporates in the still chamber. Consequently, the osmotic pressure is created between the still and the mixing chamber, and it soaks up ^{3}He in the diluted phase from the mixing chamber. At the same time, to keep the ^{3}He concentration of the diluted phase in the mixing chamber constant [20], ^{3}He crosses the boundary from the pure ^{3}He phase to the diluted ^{3}He phase, and the dilution cooling occurs at this moment.

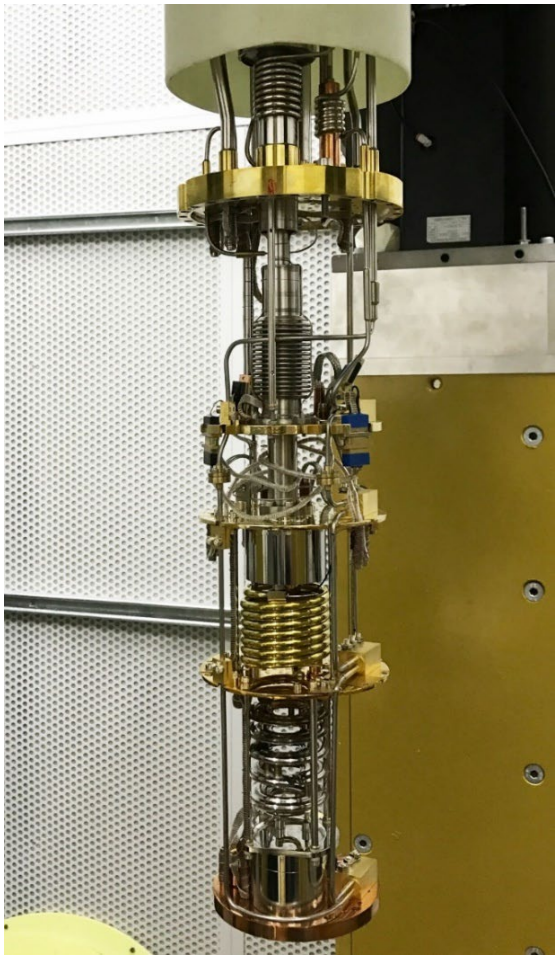

Figure 2.10: The cryostat with DR unit.

2.6. DR and Superconducting Magnet – Operation

First, we should pump out the outer vacuum chamber (OVC), that is a Dewar jacket, with a turbo pump for a week at room temperature (RT) to a pressure of low 10^{-5} $mbar$. If the vacuum of the Dewar jacket is poor, the He evaporation rate increases. As a result, frequent He refills are required, which results in a short lead time for the STM measurements.

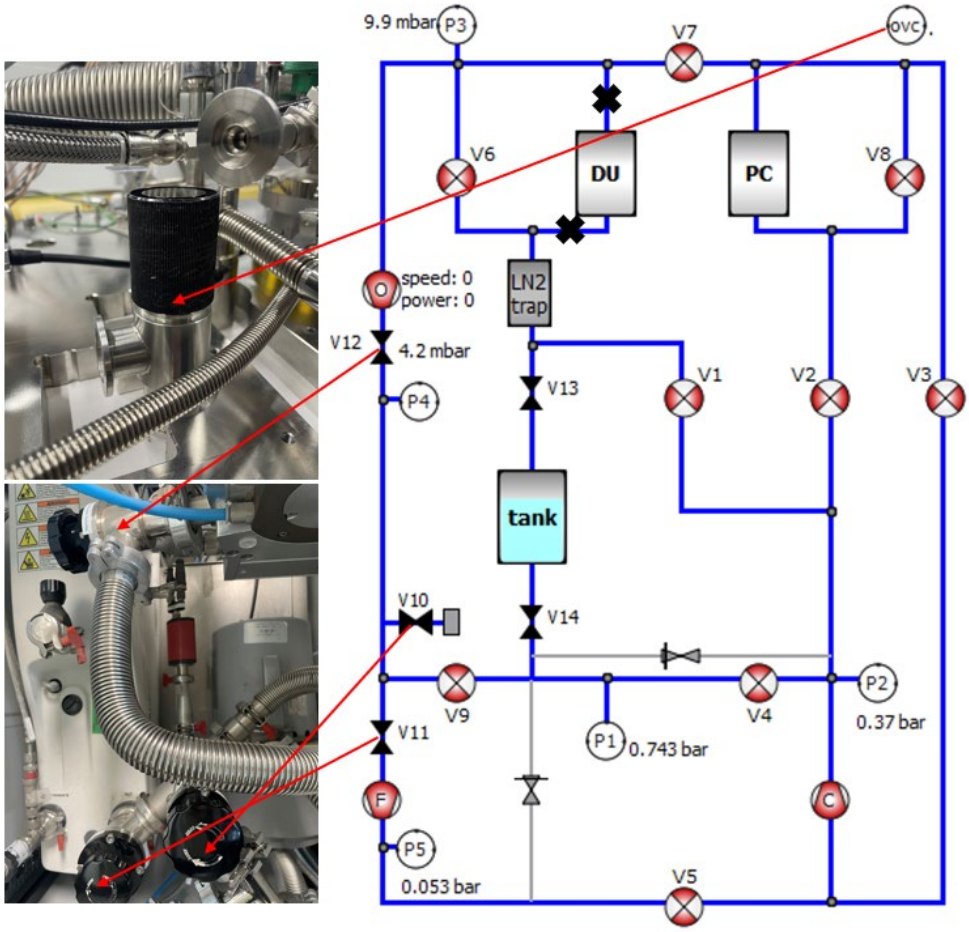

Figure 2.11: The manual valve for the OVC, the manual valves V10 –V12, and the user interface by Oxford inst.

While the OVC is being pumped out (Fig.2.11), we have to prepare a cooldown. First, we close the inner vacuum chamber (IVC) using indium sealing and pump out the IVC with a turbo pump to a pressure of high $10^{-6}\ m\mathrm{bar}$.

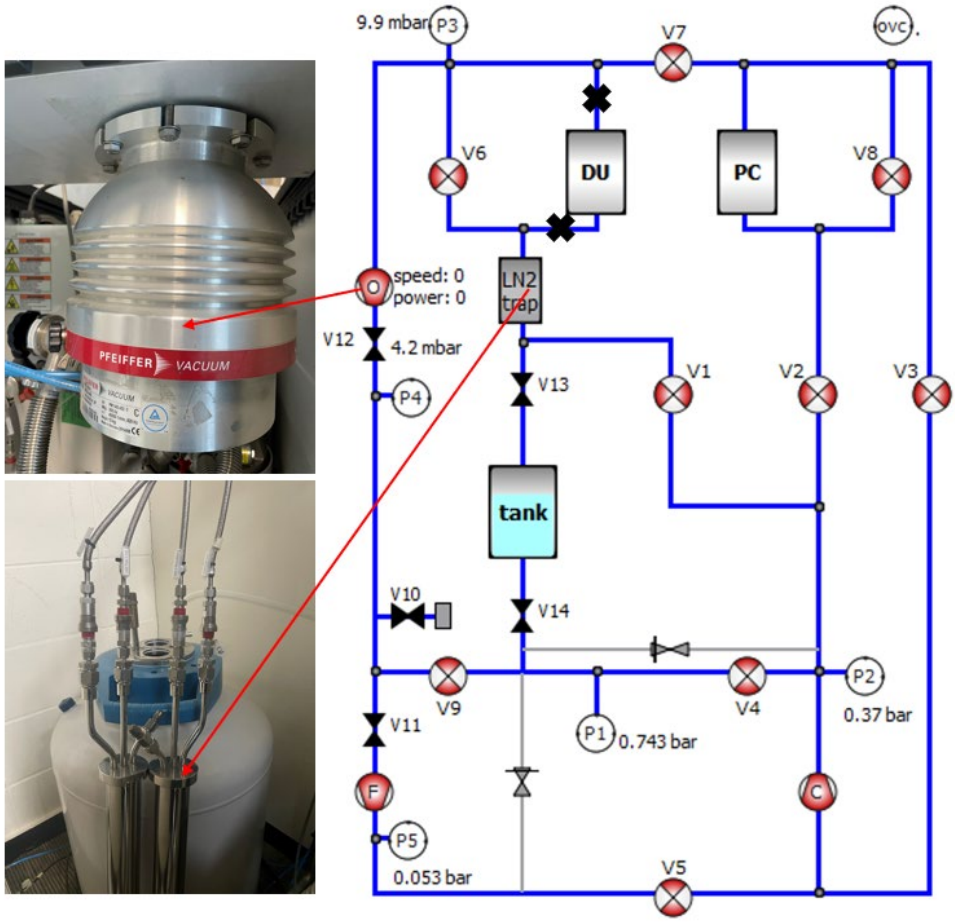

Figure 2.12: The still turbo pump, the cold traps, and the user interface.

Next, open the gate valve on the still line(Fig.2.13) and the manual valve on the condensing line(Fig.2.13). Now, the P3 goes down to a pressure of high $10^{-3}\ m\mathrm{bar}$ very slowly.

While the IVC is being pumped out, we will pump out all the mixture

gas lines overnight using the still turbo pump on the pump rack(Fig.2.12). Now, the cold traps are out of the LN_2 vessel (Fig.2.12). First, we connect a dry pump to the manual valve V10 (Fig.2.11), then start pumping and open the manual valve V10. After checking that the pressure P4(Fig.2.12) goes down to a pressure of low 10^{-1} $mbar$, open the manual valve V12 (Fig.2.11) and start the still turbo pump by selecting on the UI (Fig.2.12). After the pressure P3(Fig.2.12) goes down to a pressure of high 10^{-1} $mbar$, open the pneumatic valve V6, V7, and V8 by selecting on the UI (Fig.2.12).

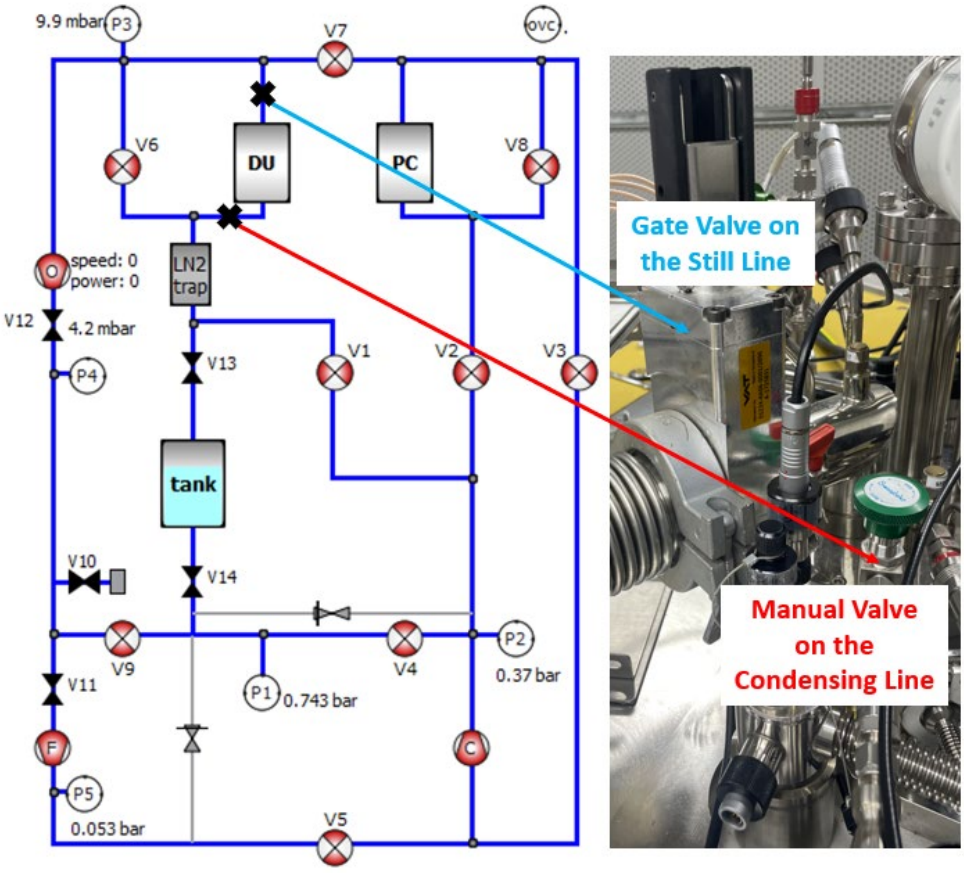

Figure 2.13: The gate valve on the still line, the manual valve on the condensing line, and the user interface.

After overnight pumping, we will stop all the pumps and close all the valves except the gate valve on the still line and the manual valve on the condensing line. First, we close the pneumatic valves V6, V7, V8, and the manual valve V10. Then, we turn off the still turbo pump, and finally close the manual valve V12 at a half maximum speed of the still turbo pump.

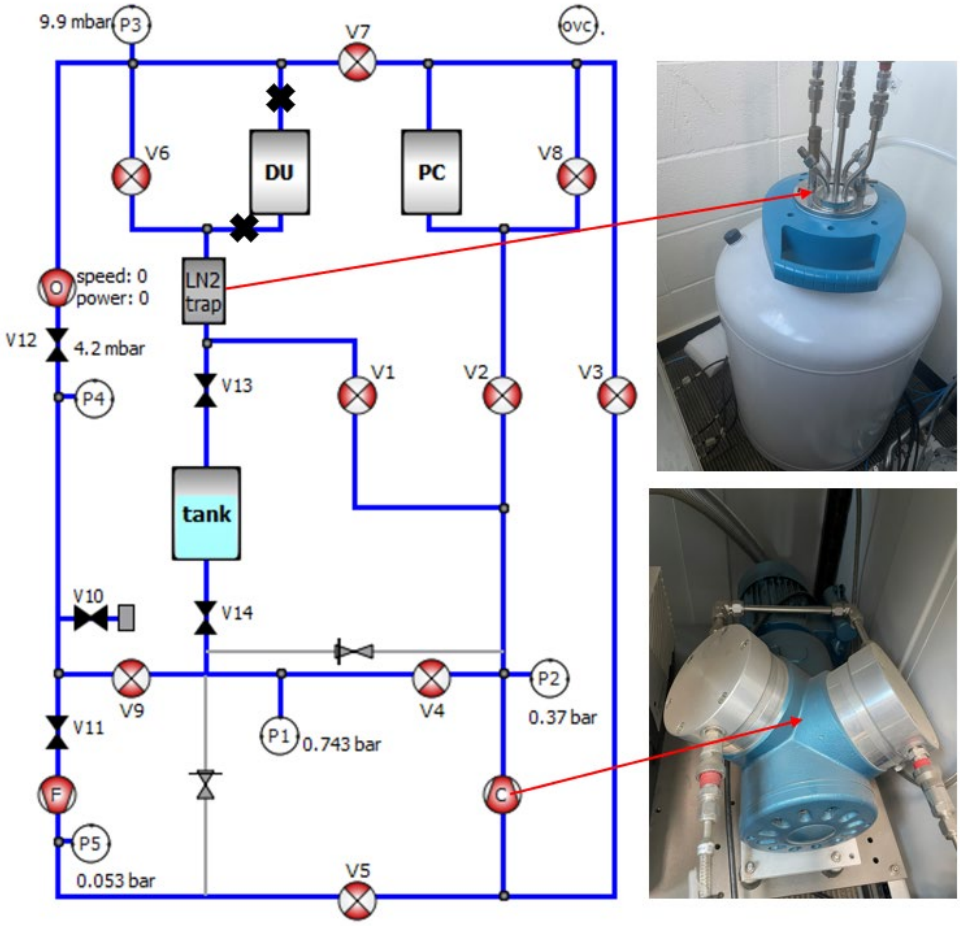

Figure 2.14: The user interface, the cold traps inside the LN_2 vessel, and the compressor.

Now, we will check out the DR unit. First, fill the vessel for cold traps with LN_2 and put the cold traps into the vessel(Fig.2.14). Then. we

start the compressor by selecting (Fig.2.14). Next, we open the manual valve V14(Fig.2.15), the pneumatic valve V4(Fig.2.13), and check the pressure P1(Fig.2.15). We should record this pressure since this is the initial tank value. Next, we connect the leak detector (LD) to the IVC and check the leak-level of the IVC when the leak-level is stabilized.

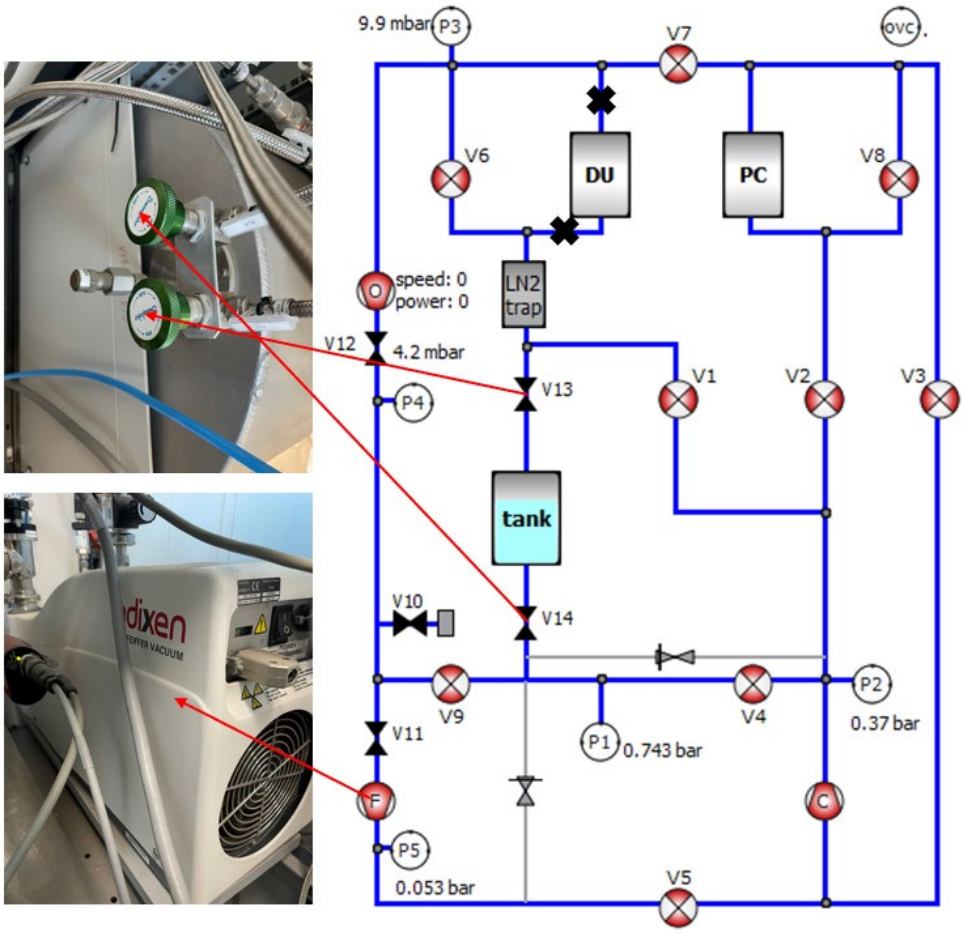

Figure 2.15: The storage tank for the mixture gas, the fore pump, and the user interface.

Now, we start the fore pump by selecting (Fig.2.15) and open the pneumatic valve V5 by selecting on the UI(Fig.2.15). Next, we

open the pneumatic valve V1 by selecting ⊗ on the UI(Fig.2.15) and check the leak-level of the IVC again. Now, the mixture gas goes into the DR unit. If there is no change of the leak-level on the LD, then we open the manual valve V11(Fig.2.15). Now, we pressurize the DU by opening and closing the pneumatic valve V9(Fig.2.15) repeatedly until the pressure P2 reaches 2.5 bar. Do not exceed the pressure P5(Fig.2.14) over 1 bar. While pressurizing the DU, we should check the leak-level of the IVC at the same time. If there is no noticeable change of the leak-level on the LD, then the condensing line and mixing chamber have no leak. This procedure is the leak-check on the condensing line at RT.

In addition, we should check that the pressure P3(Fig.2.15) increases at a constant rate and record this rate. If the rate is constant, then there is no blockage on the condensing line. This is called the throughput test at RT.

Now, we should check the still line. First, we open the pneumatic valve V4 to decrease the pressure of the DR unit until P2 reaches < 1 bar. Then, we close the V4, open the pneumatic valve V6(Fig.2.15). Now, the mixture gas goes into the still line. We check the leak level of the IVC. If there is no change of the leak-level, then we pressurize the still by opening and closing V9 repeatedly until the pressure P2 reaches 0.8 bar and the pressure P3 reaches 700 *m*bar. Never pressurize the still over 1 bar. Since the still is very sensitive and weak to the pressure, over pressurizing will cause the permanent dagame on the still. We check the leak level of the IVC again. If there is no noticeable change of the leak-level on the LD, then the still has no leak. This is the leak-check on the still line at RT.

Now, open V4 again to decrease the pressure of the still line. Next, we will collect the mixture gas to the tank. First, close V1 and open V12 very slowly. Do not exceed the pressure P5 (Fig.2.15) over $1\ \mathrm{bar}$. If the P3 reaches $10^{-1}\ m\mathrm{bar}$, turn on the still turbo pump and wait until P1 and P2 are saturated to the initial tank value. After that, we close the gate valve on the still line, the manual valve on the condensing line. The, we close V6, V14, V4, V5, and V11. Then, stop the compressor and the fore pump. Finally, stop the still turbo pump and close V12 at a half maximum speed of the still turbo pump. Now, all the valves are closed, and all the pumps are stopped. Finally, we replace the LD, which is connected to the IVC, with a dry pump. Now, the preparation for the initial cooldown is ready.

Next, we start the LN2 transfer to the He bath. Figure 2.16 provides the conditions for the magnet and the He bath. The MB1.T1.T shows the current temperature of the magnet. If the magnet temperature reaches $77\ \mathrm{K}$, we start the He exchange gas method.

Figure.2.16: The display of the magnet controller

The heat transfer in the cryostat for DR is very poor. To increase

the cooling speed of the IVC, we put a very small amount of the He gas into the IVC(Fig.2.18) up to $10^{-1}\,m\mathrm{bar}$, which acts as a heat exchange gas. Without an exchange gas, the temperature of the IVC decreases at a rate of $1\,\mathrm{K}/hour$. However, with the exchange gas method, the temperature decreases at a rate of $1\,\mathrm{K}/min$. This is a very efficient method to save time for the initial cooldown.

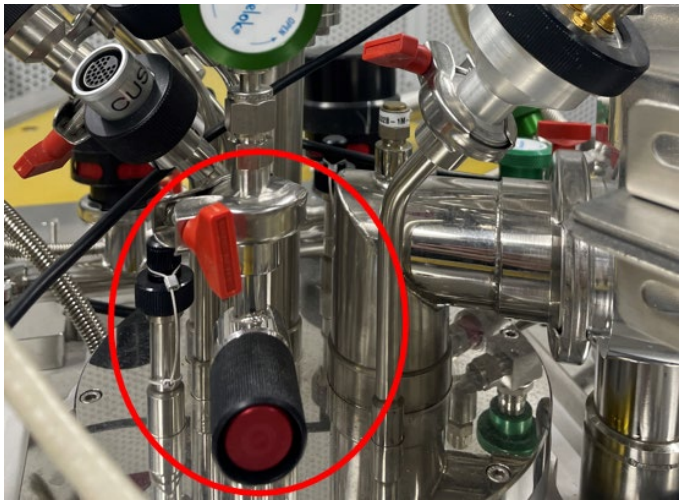

Figure.2.17: The manual valve for the IVC

After the IVC reaches $77\,\mathrm{K}$ (Fig.2.18), we pump out the IVC again to remove the He gas for overnight. Next, we start LN_2 back-transfer. Then, we flush the He bath with the He gas for five times by pumping out and purging. After that, we connect the LD to the IVC and perform the leak test on the IVC by filling the He bath with the He gas. If there is no cold leak on the IVC, then we start the DU test at the cold temperature (CT).

First. we start the compressor, the fore pump, and we open the pneumatic valve V5. Then, we open the manual valve V14 of the storage tank for the mixture gas. Next, we open the pneumatic valve

V4 and record the pressure P1. Now, the LD, which is connected to the IVC, is running. We open the pneumatic valve V1 and check the leak-level of the IVC again. If there is no change of the leak-level on the LD, then we open the manual valve V11. Now, we pressurize the DU by opening and closing the pneumatic valve V9 repeatedly until the pressure P2 reaches 2.5 bar. Do not exceed the pressure P5 over 1 bar. While pressurizing the DU, we should check the leak-level of the IVC at the same time. If there is no noticeable change of the leak-level on the LD, then the condensing line and mixing chamber have no cold leak. This procedure is the cold leak-check on the condensing line.

	name		T(K)	R(Ω)	calibration	delay	excitation
1	JT Stage		3.321	2.86 kΩ	X101282	10 sec	200 μV
2	Still Plate		1.043	6.032 kΩ	P0_RuO2	10 sec	63.2 μV
3	Cold Plate		181.7 mK	17.09 kΩ	P0_RuO2	10 sec	63.2 μV
4	Mixing Chamber (RuO2)		22.72 mK	100.3 kΩ	P0_RuO2	13 sec	200 μV
5	Mixing Chamber (Cernox)		1.213	VMIX_OVL	X101393	13 sec	200 μV

Figure 2.18: The temperature display of each stage of the DR unit.

Next, we check that the rate of pressure P3. This rate at CT should be larger than six to eight times the rate at RT. If not, there might be a blockage. This is called the throughput test at CT.

Now, we check the still line. We open the pneumatic valve V4 to decrease the pressure of the DR unit until P2 reaches < 1 bar. Then, we close the V4, open the pneumatic valve V6. We check the leak level of the IVC. If there is no change of the leak-level, then we pressurize the still by opening and closing V9 repeatedly until the

pressure P2 reaches $0.8\,\mathrm{bar}$ and the pressure P3 reaches $700\,m\mathrm{bar}$. Never pressurize the still over $1\,\mathrm{bar}$. We check the leak level of the IVC again. If there is no leak, then the still has no leak at CT. This is the cold leak−check on the still line.

After the DR unit test, we collect the mixture gas to the tank. While collecting, we start the initial LHe transfer to the He bath. First, we transfer LHe under the pressure of $1\,\mathrm{psi}$. After the magnet temperature reaching $4\mathrm{K}$, we pressurize the LHe storage Dewar up to $3\,\mathrm{psi}$. Then, we put the He gas into the IVC again. If the temperatures of the cold plate and mixing chamber plate reaches $<$ $20\,\mathrm{K}$ (Fig.2.18), pump out the IVC again using the turbo pump.

Then, we start the second LHe transfer and stop the still turbo pump on the pump rack. Finally, we select "start the condensing" on the menu bar of the UI (Fig.2.19). Then the DR unit starts condensation. The base temperature of our system is about $22\,m\mathrm{K}$ (Fig.2.18). If we want to stop the DR cooling, then select "collect the mixture" on the menu bar of the UI. After the temperature of DR unit reaches above $20\,\mathrm{K}$, close all the valves and stop all the pumps.

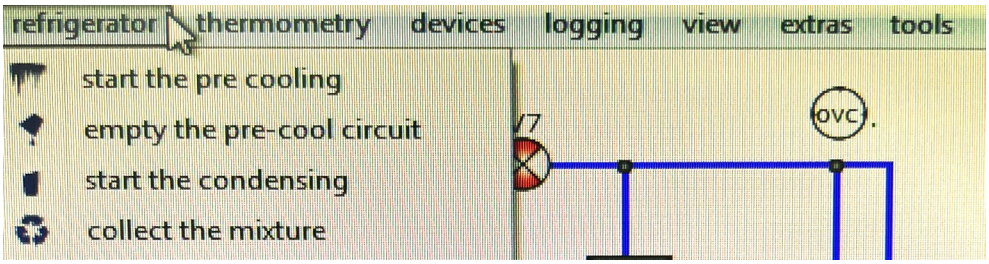

Figure 2.19: The DR user interface by Oxford Inst.

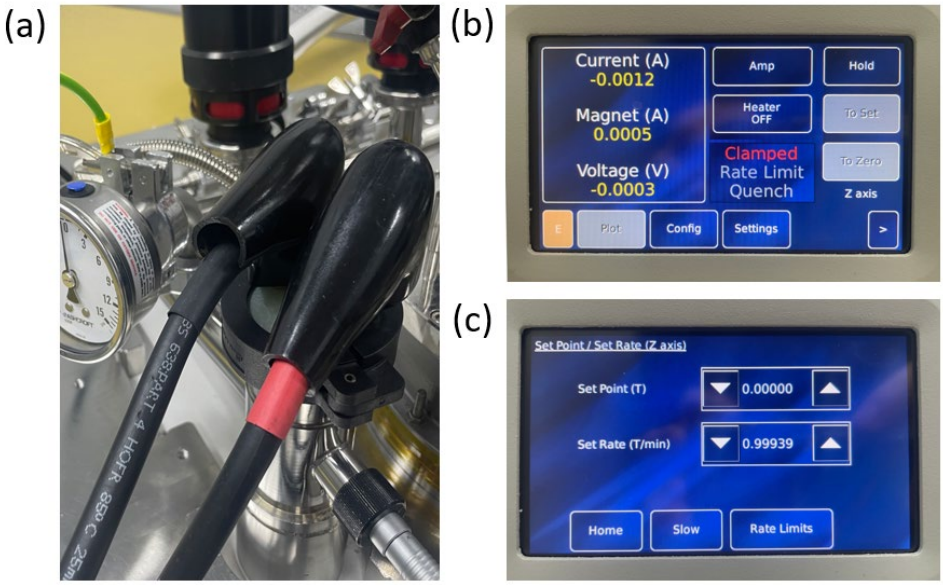

Figure 2.20: The magnet lead cables and the magnet user interface.

Now, we will operate the 14T magnet. We should connect the magnet lead cables from the power supply to the Dewar (Fig.2.20(a)). The fig.2.20(b) and (c) is the user interfaces by Oxford inst. First, we press "Hold"(Fig.2.20(b)), then the magnet power supply is ready to energize. Next, turn on the switch heater(Fig.2.20(b)). Now, the magnet in superconducting state inside the He bath is electrically connected to the power supply. Then, enter the target tesla on the "Set Point (T)"(Fig.2.20(c)) and $6\,\mathrm{A}/min$ on the "Set Rate" (Fig.2.20(c)). The mode should be "slow"(Fig.2.20(c)). Next, press "To Set"(Fig.2.20(a)), then it starts energizing. If the magnet reaches its target tesla, then the color of "Hold" turns into yellow. Next, we should turn off the switch heater and select "To Zero"(Fig.2.20(b)). After "Hold" is on, the magnet is in the persistent mode.

Now, we will turn off the magnet, First, enter the previous target

tesla on the “Set Point (T)”. Then, press “To Set”. After the reaching the target tesla, the “Hold” is ON. Next, we turn on the switch heater and enter zero into “Set Point” and “$7.22\ \mathrm{A}/min$” into “Set Rate”. Now, we change the mode into the “Fast” mode by selecting (Fig.2.20(c)). Next, we press “To Zero”, and the current from the magnet decreases to the zero. After the “Hold” is on, we should turn off the switch heater. Finally, push the power button.

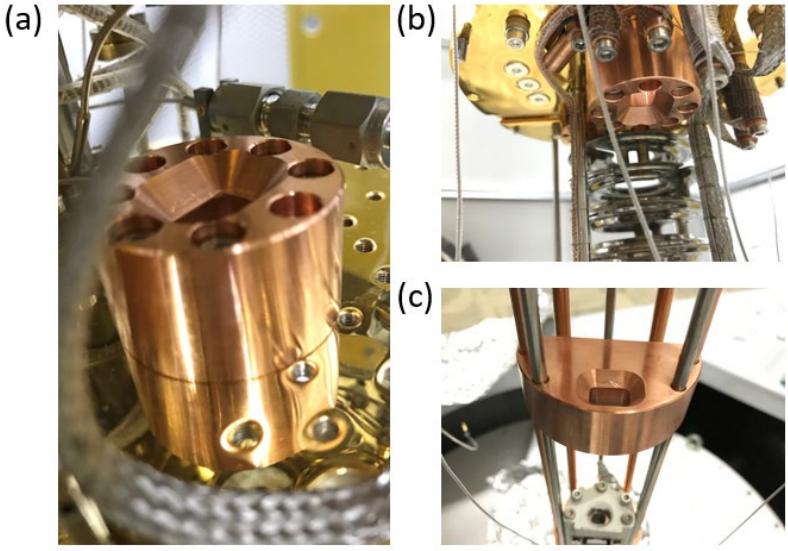

Figure 2.21: The keyholes for the sample transfer rod.

Next, we will explain the sample transfer procedure. The transfer rod system consists of three stages. After the sample is attached on the stud, the rod is installed on the top flange of the IVC. Then we pump out the chamber for the sample stud to the pressure of $5 \times 10^{-6}\ m\mathrm{bar}$. Then, we lower the transfer rod into the IVC, until it touches down the 4K plate. While lowering the rod, we assemble all the stages of the sample transfer rod. If it arrives at 4K plate, we raise the rod slightly and wait for 1 hour. After that, we cleave the

sample by pushing and rotating. If the sample is cleaved, we lower down the rod to the STM Head. During lowering the rod, it passes through the three key holes before reaching the STM head. If the rod is stopped, then we rotate the rod to pass the keyhole. The transfer rod should pass through the three keyholes to reach the STM head. The first keyhole(Fig.2.21(a)) and the second keyhole(Fig.2.21(b)) are mutually perpendicular. Similarly, the second keyhole and the third keyholes(Fig.2.21(c)) are mutually perpendicular. Since the rod is too long, the keyholes act as guides.

2.7. Summary

1. Preparation

    1. Pump out the outer vacuum chamber (OVC) with turbopump over one week at room temperature (RT).
    2. Supply water through the cooling line of the turbopump.
    3. Supply N_2 gas to the gas handling system up to 6 bars.
    4. Check all the mixture and electric line connections.

2. Day I

    1. Pump out all the mixture gas lines of DR and precool area through V10 overnight.

3. Day II

    1. Inner vacuum chamber (IVC) leak check at RT

2. Mixture line leak check at RT
3. Finish pumping out mixture gas lines and close all the valves except the green valve and the gate valve.
4. Put the cold traps into the LN_2 Dewar.
5. Throughput test: pressurize DR unit up to P2 ~ 2.5bar and check the pressure increase of P3.
6. Check the leak level while pressurizing P2.
7. Close V1, open V4, and open V1 again.
8. Open V6 and pressurize the still up to P2~0.8bar and P3~700mbar.
9. Check the leak level.
10. Collect mixture to the tank
11. LN_2 transfer to the Dewar
12. Put a small amount of ^{4}**He** exchange gas into IVC.
13. LN_2 back-transfer from the Dewar.
14. Throughput test again at 77K.
15. Still line leak check again at 77K.
16. Collect mixture gas to the tank.
17. LHe transfer to the Dewar
18. Under 20 K of DR unit, start condensing to achieve base temperature while pumping IVC with turbopump.

4. Operation of magnet

1. Turn on the switch heater. Then, the superconducting wire turns into normal state.
2. Energize the magnet up to target tesla (Maximum: 14 T).
3. Turn off the switch heater.
4. Lower down the current of power supply to zero ampere.

5. Give the same current with the previous one.
6. Turn of the switch heater.
7. Lower down the current to zero ampere.
8. Turn off the switch heater.

Chapter 3.

Cuprate Superconductors

In 1911, the Heike Kamerlingh Onnes discovered that the resistivity of mercury disappeared at 4.2K [23]. This phenomenon is called superconductivity. One of the peculiar properties of the superconductor is a perfect conductor.

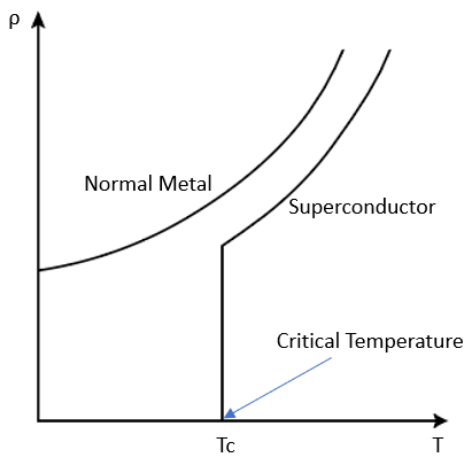

Figure 3.1: The comparison of normal metal and superconductor

In 1933, Meissner and Ochsenfeld found that the superconductors expelled the magnetic flux, which is known as Meissner effect [24]. This is the other property of superconductors, which is perfect diamagnetism.

Many theoretical efforts to explain superconductivity have been made. Especially, John Bardeen, Leon N. Cooper, and Robert

Schrieffer successfully developed the microscopic description for the conventional superconductors [27], which describes that the superconductivity is originated from the condensation of the Cooper pairs.

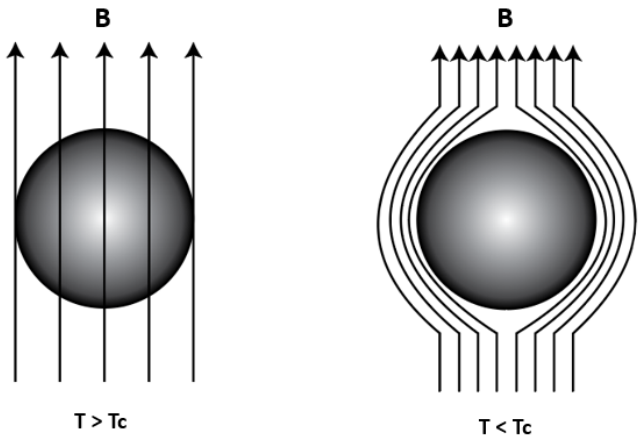

Figure 3.2: Meissner effect

However, after the discovery of a new type of superconductors in 1986 [28], which is not explained by BCS theory, there has been no consensus that a complete theoretical description has been developed until now.

3.1. Brief History of Superconductivity

After the success of helium liquefaction by Heike Kamerlingh Onnes in 1908, he investigated the resistivity of pure metals at low temperature. Meanwhile, he discovered that the electrical resistance of solid mercury in liquid helium vanished in 1911 [23]. This is the first discovery of superconductivity. After that, the same phenomena were discovered in other metals.

Many theoretical efforts had been made to elucidate the phenomenon. Among them, London theory [25] and Ginzburg−Landau theory [26] are still elucidating. The complete microscopic description of superconductivity was developed by John Bardeen, Leon N. Cooper, and Robert Schrieffer in 1957 [27].

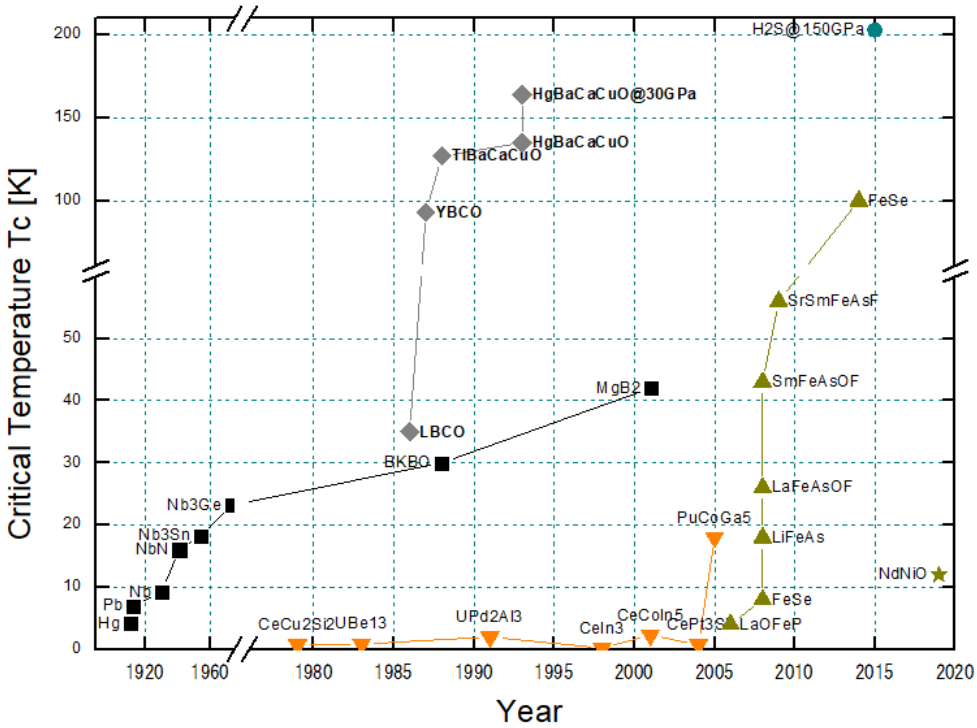

Figure 3.3: The history of superconductors

The history of superconductors with their discovery years and transition temperatures

However, a totally new kind of superconducting material, which is not explained by the BCS theory, was found in the compound $La_{2-x}Ba_xCuO_4$ with $T_c \sim 35\,K$ by Bednorz and Muller in 1986 [28]. This is a cornerstone of high−temperature superconductor. In the subsequent year, another high−temperature superconductor $YBa_2Cu_3O_{7-x}$ was found and its critical temperature is $T_c \sim 93\,K$ [29], which is higher than liquid nitrogen temperature. In 1988, another

high−temperature superconductor $Bi_2Sr_2CaCu_2O_{8+x}$ was found with $T_c \sim 105\,K$ [30]. All these materials are copper oxide superconductors, which are called cuprate superconductors. In 2006, another kind of superconductor LaOFeP with $T_c \sim 4\,K$ is found [31], which is an iron−based superconductor. The H_2S under high pressure shows superconductivity with $T_c \sim 203\,K$ [32]. Figure 3.1 shows a brief history of superconductors with their critical temperature and discovered years.

3.2. Cuprate Superconductors

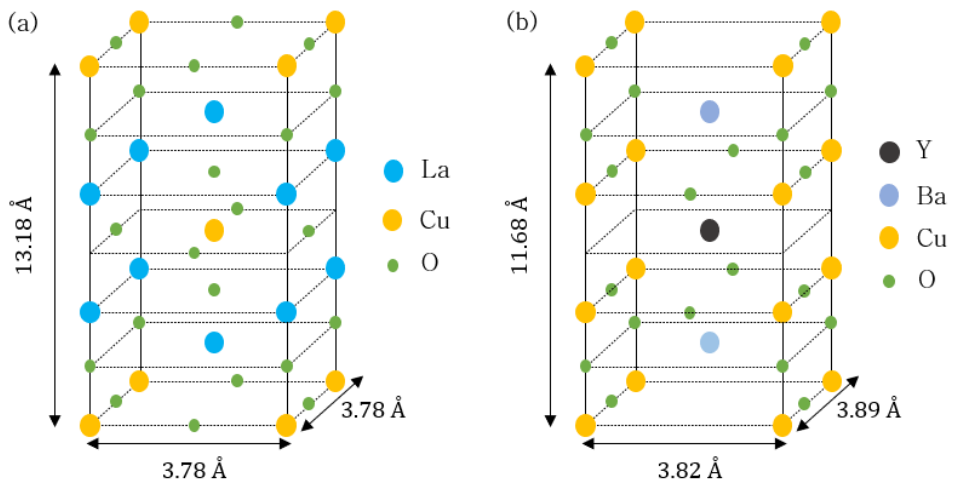

Figure 3.4: Crystal structures of the cuprate superconductors
(a) $La_{2-x}Ba_xCuO_4$ (b) $YBa_2Cu_3O_{7-x}$

In 1986, J. Georg Bednorz and K. Alexander Müller discovered superconductivity in an oxide material, that is $La_{2-x}Ba_xCuO_4$ with $T_c \sim 35\,K$ [28]. This is a breakthrough since it is unconventional superconductor which is not explained by the BCS theory. In 1987, another high−Tc superconductor $YBa_2Cu_3O_{7-x}$ with $T_c \sim 93\,K$ was

discovered [29]. This is the first superconductor whose critical temperature exceeds the boiling point of liquid nitrogen. The cuprate superconductors are perovskite structures with copper oxide planes separated by other metal oxide layers. The superconducting phenomena are believed to happen in the copper oxide layers. The dopants are introduced to other adjacent layers, which act as charge reservoirs that provide electrons (or holes) into the copper oxide layers.

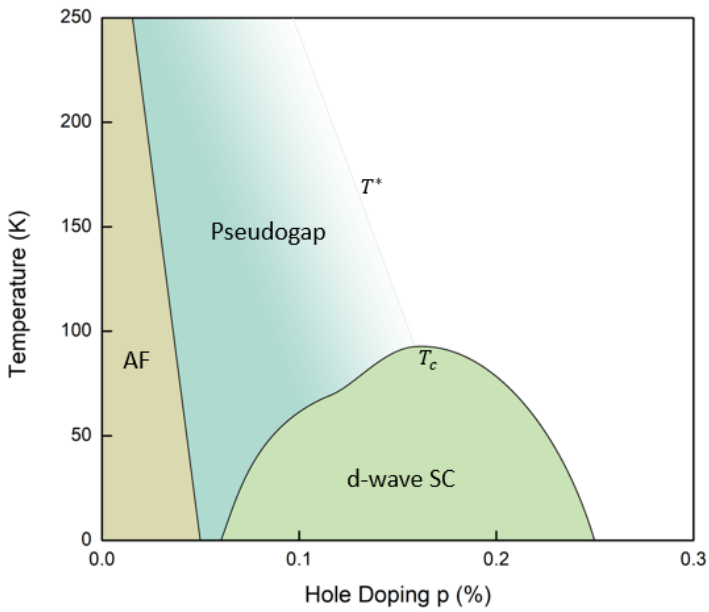

Figure 3.5 Schematic phase diagram of high−Tc cuprates

3.3. $\mathbf{Bi_2Sr_2CaCu_2O_{8+x}}$

In 1988, Hiroshi Maeda discovered another type of cuprate superconductor without containing rare earth elements, which is bismuth strontium calcium copper oxide (BSCCO) with $T_c \sim 105\,K$ [30].

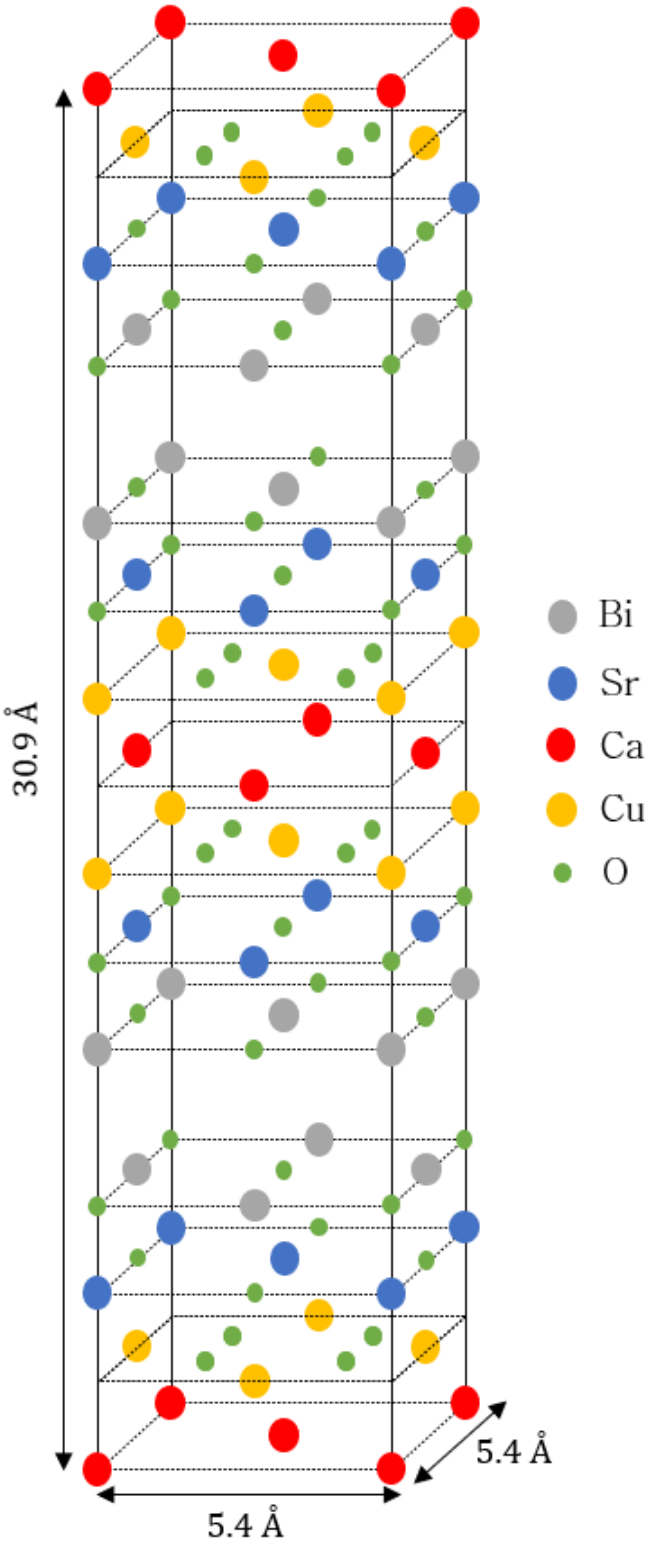

Figure 3.6: Crystal structures of $\mathbf{Bi_2Sr_2CaCu_2O_{8+x}}$

In this thesis, we especially investigate $\mathbf{Bi_2Sr_2CaCu_2O_{8+x}}$ among several members of BSCCO. The bonding between two adjacent BiO planes is weak. By *in−situ* cleaving inside the vacuum chamber, the BiO surface is exposed. The cleaved surface is very clean and atomically flat compared to other materials. Fig.3.6 shows the real cleaved $\mathbf{Bi_2Sr_2CaCu_2O_{8+x}}$ sample and its crystal structure is shown in Fig.3.6.

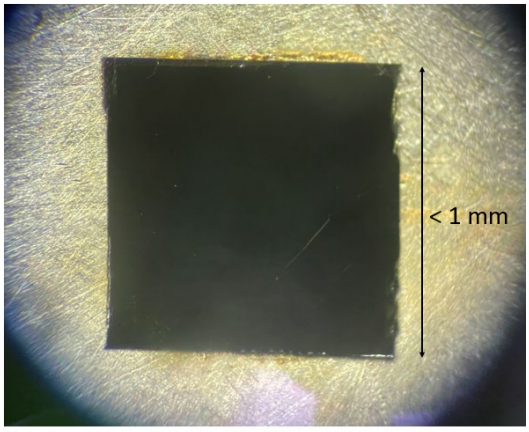

Figure 3.7 : Cleaved $\mathbf{Bi_2Sr_2CaCu_2O_{8+x}}$ sample

Chapter 4.

Spectroscopic Imaging Scanning Tunneling Microscopy at $25\,m$K

4.1. Scanning Tunneling Microscopy at $\mathbf{4.2\,K}$

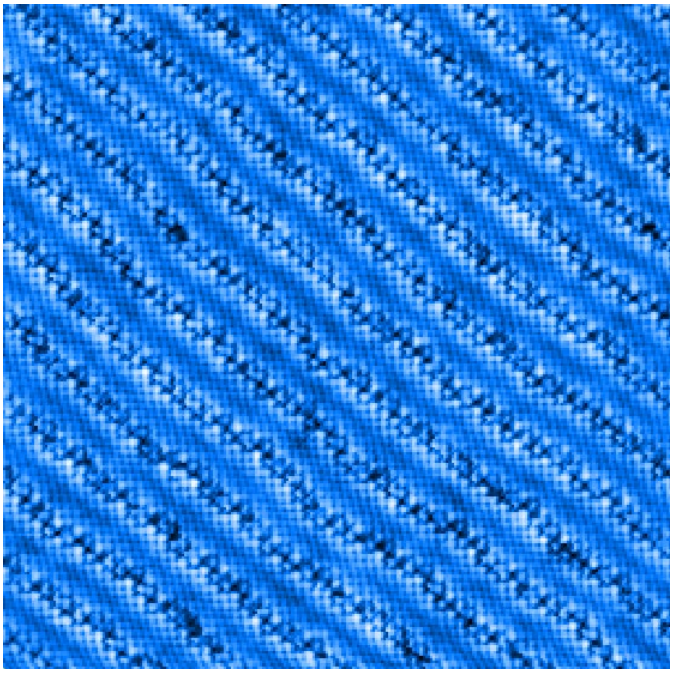

Figure 4.1: Topographic image of $\mathbf{Bi_2Sr_2CaCu_2O_{8+x}}$ at $\mathbf{4.2\,K}$

Topographic image of $Bi_2Sr_2CaCu_2O_{8+x}$ measured by tungsten tip at $4.2\,K$ using DR−STM $(30nm \times 30nm,\ V = 100\,mV,\ I = 40\,pA)$

We have measured the $Bi_2Sr_2CaCu_2O_{8+x}$ sample by tungsten tip at

4.2 K using DR−STM. Fig.4.1 shows its topographic image. We have demonstrated that our DR−STM shows atomic resolution. Also, we performed spectroscopic measurements on $Bi_2Sr_2CaCu_2O_{8+x}$ by tungsten tip using DR−STM. From this spectrum, the superconducting gap is clearly seen.

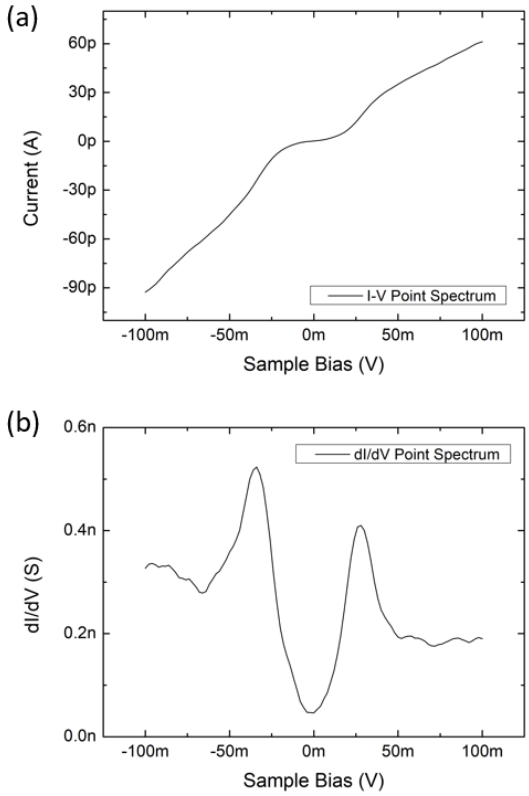

Figure 4.2: Point spectra of $Bi_2Sr_2CaCu_2O_{8+x}$

(a) $I-V$ point spectrum (b) dI/dV point spectrum

4.2. Scanning Tunneling Microscopy at $25\,mK$

In Fig.4.3, we have measured the $Bi_2Sr_2CaCu_2O_{8+x}$ sample by tungsten tip at $25\,mK$ using DR−STM. It still shows atomic resolution

well, even if we compare to the topographic image in Fig.4.1.

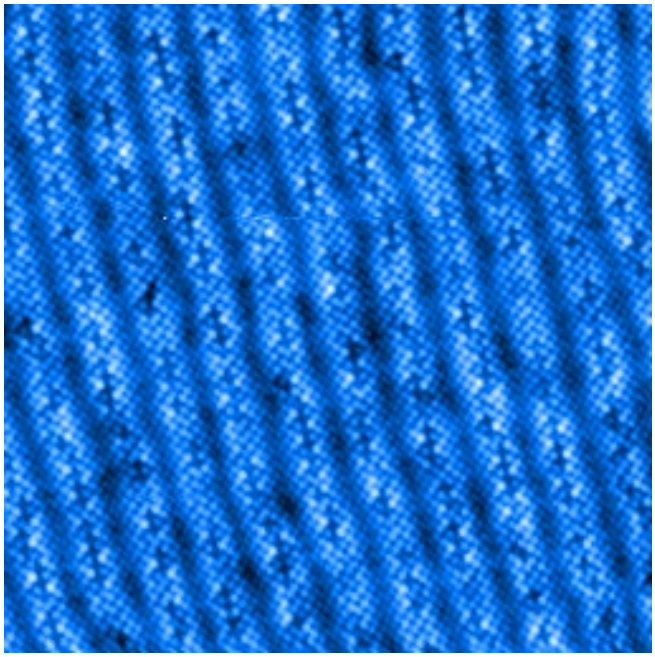

Figure 4.3: Topographic image of $\mathbf{Bi_2Sr_2CaCu_2O_{8+x}}$ at $\mathbf{25\,mK}$

Topographic image of $Bi_2Sr_2CaCu_2O_{8+x}$ measured by tungsten tip at $25\,mK$ using DR−STM $(30\,nm \times 30\,nm,\ V = 100\,mV,\ I = 10\,pA)$.

Fig.4.4 shows spectroscopic measurements of $Bi_2Sr_2CaCu_2O_{8+x}$ sample at $25\,mK$ and $13\,T$. Fig.4.4(a) is a topographic image measured by a tungsten tip. Fig.4.4(b) shows a differential conductance map which shows vortex features. Fig.4.4(c) shows the gap map and its gap size distribution is in Fig.4.4(d). Finally, Fig.4.4(e) shows dI/dV point spectra for the linecut in (c). From this measurement, we have fully demonstrated the performance of DR−STM with its spectroscopic measurement ability at mK temperature and under the high field magnet.

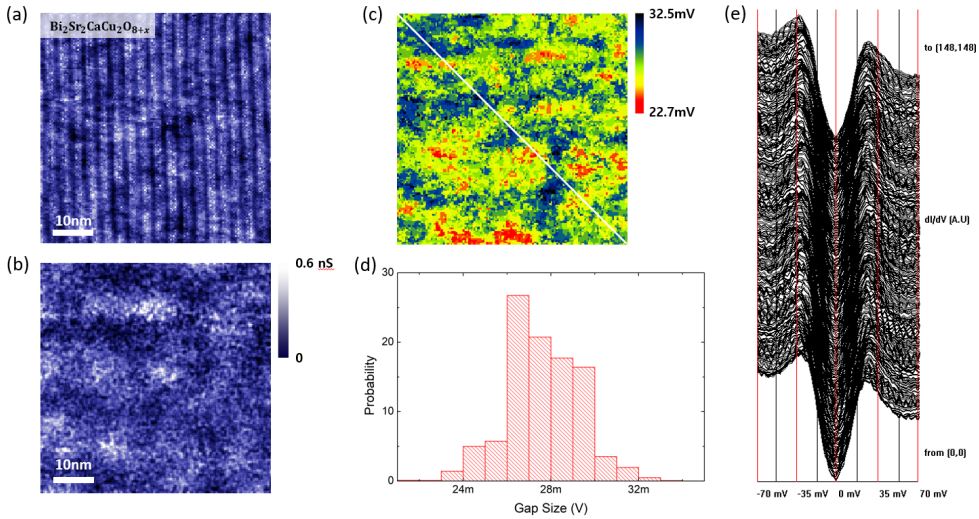

Figure 4.4: Spectroscopic measurements of $\mathbf{Bi_2Sr_2CaCu_2O_{8+x}}$ at 25 mK

(a) Topographic image of $Bi_2Sr_2CaCu_2O_{8+x}$ measured by tungsten tip at 25 mK and 13 T using DR-STM $(60\,nm \times 60\,nm,\ V = 70\,mV,\ I = 40\,pA)$ (b) Differential conductance map of the same region (c) Gap map of the same region (d) Gap size distribution (e) dI/dV point spectra along the line profile in (c).

4.3. SIS Tunneling Microscopy

In conventional STM measurement, we use normal metal tip. However, in this measurement, the $Bi_2Sr_2CaCu_2O_{8+x}$ tip is fabricated *in-situ*. Fig.4.5 shows topographic image measured by this $Bi_2Sr_2CaCu_2O_{8+x}$ tip. The atomic corrugations are resolved by convolution of tip and sample.

$$(f * g)(\boldsymbol{r}) = \int_{-\infty}^{\infty} f(\boldsymbol{r}) g(\boldsymbol{r} - \boldsymbol{R}) dR$$

Fig.4.6(a) shows topographic image measured by normal metal tip

and SIN tunneling happens in this measurement. However, Fig.4.6(b) shows topographic image measured by $Bi_2Sr_2CaCu_2O_{8+x}$ tip and SIS tunneling happens in this measurement.

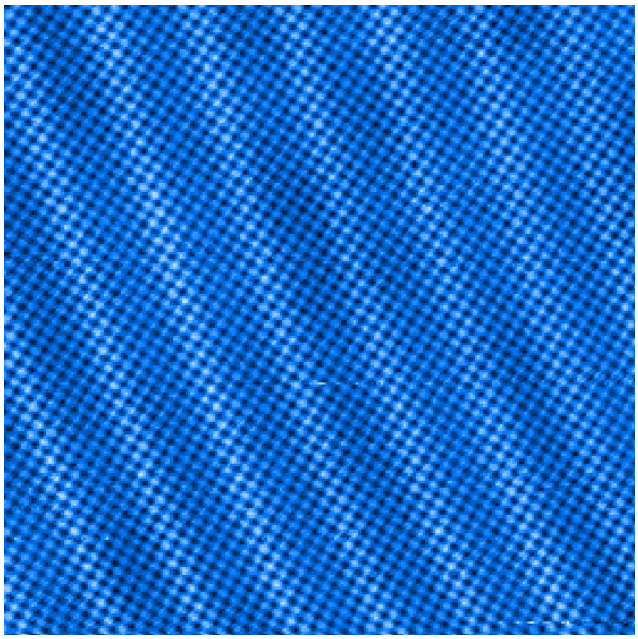

Figure 4.5: Topographic image of $Bi_2Sr_2CaCu_2O_{8+x}$ by SIS tunneling

Topographic image of $Bi_2Sr_2CaCu_2O_{8+x}$ measured by $Bi_2Sr_2CaCu_2O_{8+x}$ tip at 25mK using DR−STM ($20\,nm \times 20\,nm,\ V = 100\,mV,\ I = 20\,pA$).

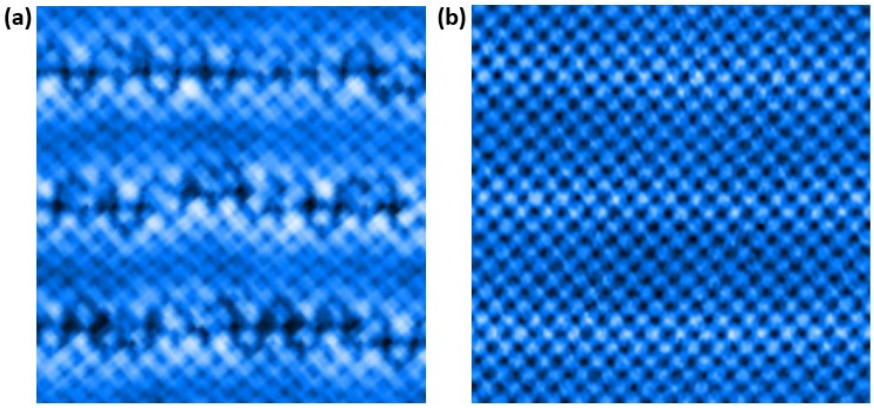

Figure 4.6: Comparison of topographic images of $Bi_2Sr_2CaCu_2O_{8+x}$ by SIN tunneling and SIS tunneling.

Chapter 5.

Single Electron Tunneling Spectroscopy at 25 mK

5.1 Coulomb Blockade and Single Electron Tunneling

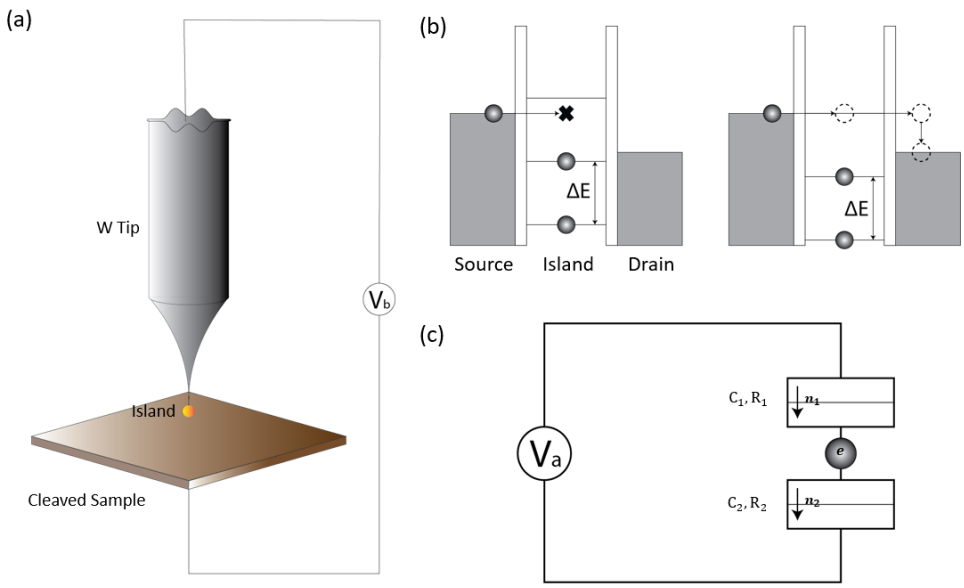

Figure 5.1: Coulomb blockade tip and single electron tunneling.
(a) Schematic of STM measurement with Coulomb blockade tip. (b) Energy diagram of a single−electron transistor (c) Circuit model corresponding to a single−electron transistor.

In this chapter, we measured $Bi_2Sr_2CaCu_2O_{8+x}$ sample using the special probe tip, which was created *in−situ*. In general, a normal metal tip (e.g., tungsten tip) is used for the conventional STM

measurement. In the previous chapter, we investigated other type of probe tip ($Bi_2Sr_2CaCu_2O_{8+x}$−tip), which was fabricated *in−situ*.

First, we need to characterize the tip that we used for our measurement. Figure 5.1(a) shows the schematic picture of Coulomb blockade tip for our measurement. A tiny island is attached to the end of the tungsten tip, which was created during tip treatment on the gold sample. This small island creates a double barrier structure. Figure 5.1(b) describes this tip using the single−electron transistor model. If the Fermi level of the source is equivalent to the empty energy level of the island, then electron can be transmitted. However, if the energy levels are not equal, then there is no current flow. The energy gap ΔE corresponds to the capacitance $C = e^2/\Delta E$ of the island. Figure 5.1(c) explains this transistor as a circuit model [33]. This is a single electron transistor. In other words, we created an extremely charge−sensitive tip for our STM measurement.

5.2. Single Electron Tunneling (SET) Spectroscopy

Figure 5.2(a) shows the $\mathrm{I}-\mathrm{V}$ point spectrum of $Bi_2Sr_2CaCu_2O_{8+x}$ and its $d\mathrm{I}/d\mathrm{V}$ spectrum measured by tungsten tip. The superconducting gap is clearly seen from this $d\mathrm{I}/d\mathrm{V}$ spectrum. However, for the measurement in Fig.5.2(b) using our special Coulomb blockade tip, which is extremely charge sensitive, step feature is shown on the $\mathrm{I}-\mathrm{V}$ point spectra. Also, $d\mathrm{I}/d\mathrm{V}$ spectrum shows periodic peaks which are originated from step features. In Fig.5.2(c), we focused on a few steps by raising energy resolution. It shows that the width of one step is about $\Delta V \cong 0.3 m\mathrm{eV}$ and this corresponds to capacitance $0.5 f\mathrm{F}$

of the island according to the Coulomb blockade model.

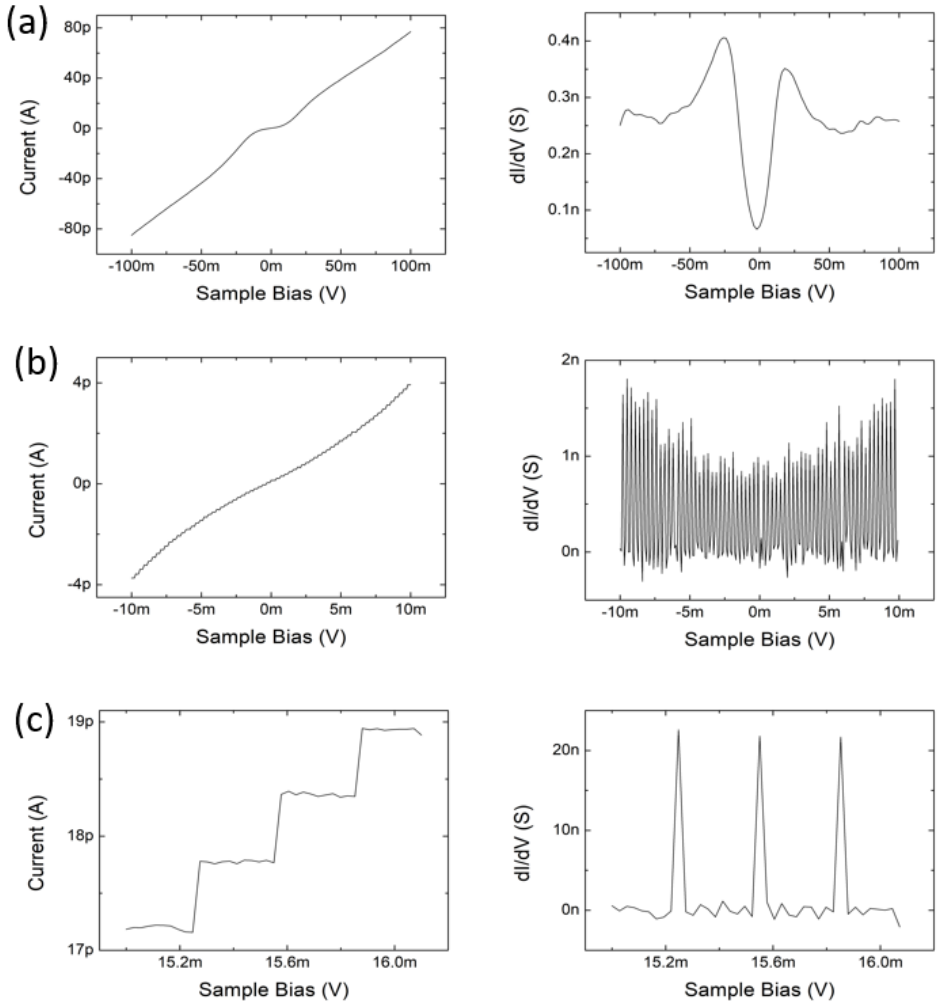

Figure 5.2: Comparison of spectroscopic measurements using normal metal tip and Coulomb blockade tip

(a) $\mathrm{I-V}$ point spectrum for Bi−2212 using normal metal tip (left) and its $d\mathrm{I}/d\mathrm{V}$ spectrum (right) (b) Wide range of $\mathrm{I-V}$ point spectrum for Bi−2212 using Coulomb blockade tip (left) and its $d\mathrm{I}/d\mathrm{V}$ spectrum (right) (c) Narrow range of $\mathrm{I-V}$ point spectrum for Bi−2212 using Coulomb blockade tip (left) and its $d\mathrm{I}/d\mathrm{V}$ spectrum (right)

5.3. SET Spectroscopic Measurement I

We measured $Bi_2Sr_2CaCu_2O_{8+x}$ sample from $-5\,meV$ to $-3.5\,meV$ at $25\,mK$ and $13\,T$. Fig.5.3(a) is a differential conductance map at $-3.65\ meV$, and it shows clear vortex features. We made masks for vortex and non-vortex. We applied these masks to the differential conductance map, and we spatially averaged spectra. This result is shown in Fig.5.3(b). The averaged spectra from each masked map show a clear distinction between them. From this result, we decided to investigate the vortex feature using the single electron tunneling spectroscopic measurement.

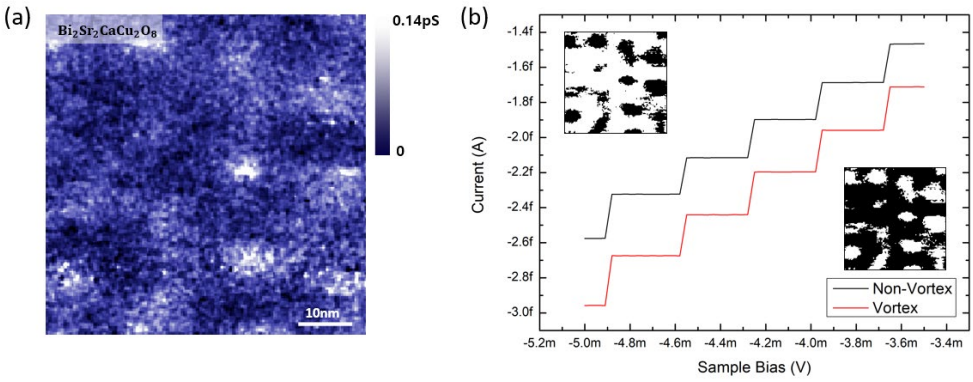

Figure 5.3: Spectroscopic measurement of $Bi_2Sr_2CaCu_2O_{8+x}$ from $-5\,meV$ to $-3.5\,meV$ at $25\,mK$ and $13\,T$

(a) Differential conductance map at $-3.65\ meV$ (b) Comparison of spatially averaged spectra between non-vortex area with its mask (left inset) and vortex area with its mask (right inset)

5.4. Vortex Charge

The predictions for the trapped charges in the vortices in the

superconductor have been made theoretically. Since the cuprate superconductor has a large superconducting gap compared to its Fermi energy, this system is considered as a good candidate for the measurement of vortex charges [34−36].

Many efforts for finding evidence of vortex charge in cuprate superconductors have been made in past. Among them, there are reversal of the Hall coefficient sign, vortex lattice melting, or nuclear quadrupole resonance [37−39], but they are all indirect evidence. Another piece of evidence for the vortex charge has been suggested using microwave cavity recently [39].

There can be a chemical potential mismatch at the interface between the normal region and the superconducting region [35]. Then, spectroscopic measurement using SI−STM is a good candidate to probe this phenomenon. We have investigated the possible charge accumulation around the vortices on Bi−2212 at 25mK and 13T using our SI−STM with a special single electron tunneling tip.

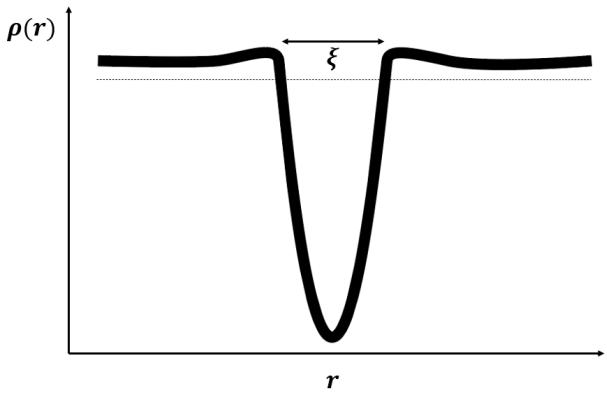

Figure. 5.4: Schematic of electron density redistribution at vortex core

Figure 5.4 shows the electron density redistribution around the vortex [40−42]. The dashed line is the average charge density. Since the electrons prefer to form a Cooper pair outside the vortex, the charge density inside the vortex is lower and the leaving electrons screens the vortices.

5.5. SET Spectroscopic Measurement II

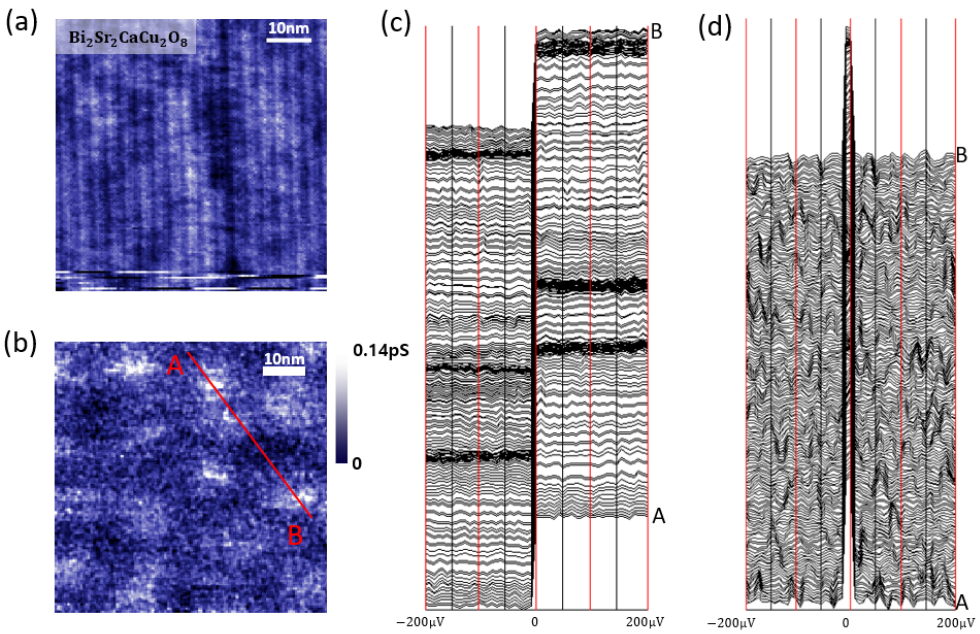

Figure 5.5: Spectroscopic measurement of $Bi_2Sr_2CaCu_2O_{8+x}$ from $-0.2\ meV$ to $0.2\ meV$ at $25\ mK$ and $13\ T$.

(a) Topographic image of $Bi_2Sr_2CaCu_2O_{8+x}$ at $25\ mK$ and $13\ T$ $(60\ nm \times 60\ nm,\ V = 100\ mV,\ I = 200\ pA)$ (b) Differential conductance map of the same region (c) I−V line profiles from A to B (d) Differential conductance spectra from A to B.

We measured $Bi_2Sr_2CaCu_2O_{8+x}$ sample from $-200\,meV$ to $200\,meV$ at $25\,mK$ and $13\,T$. Fig.5.5(a) is the topographic image of $Bi_2Sr_2CaCu_2O_{8+x}$ and Fig.5.5(b) is the differential conductance map, which shows vortex features. Fig.5.5(c)is the I−V line profile in (b), which shows the step features. However, we could not find the any displacement of steps. Fig.5.5(d) shows its differential dI/dV spectra, which shows no displacement of the peaks.

A clear shift of the CB steps was not detected possibly due to an extremely small ΔV between the steps. Theoretically predicted vortex charge per unit cell is of an order of $10^{-6}\,e$ in HTSC [36]. Estimating one vortex covers 10 unit cells, the above prediction, according to the Ginzburg−Landau theory, suggests about $300\,\mu V \times 10 \times 10^{-6} \sim 3 \times 10^{-3}\,\mu V$ of shift in Coulomb blockade step voltage which is above our energy resolution even at $25\,mK$.

Now, we focus on the one−step change with an extremely high energy resolution. In this measurement, the vortex features are still clearly seen, and we found spatially averaged spectra for the vortex region and non−vortex region using masks. In Fig.5.6(c), there is a tiny difference between the two spectra.

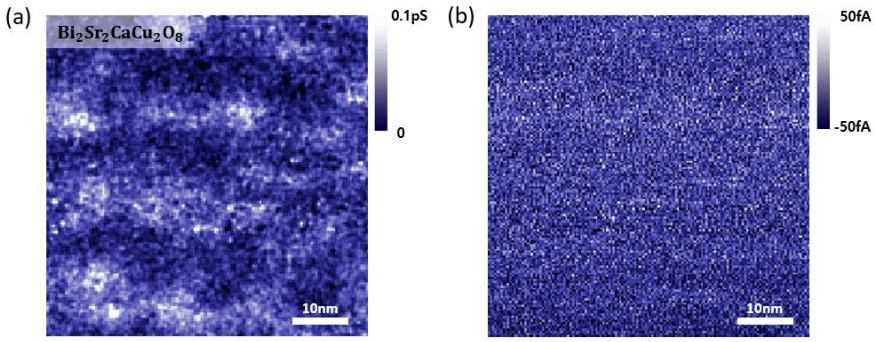

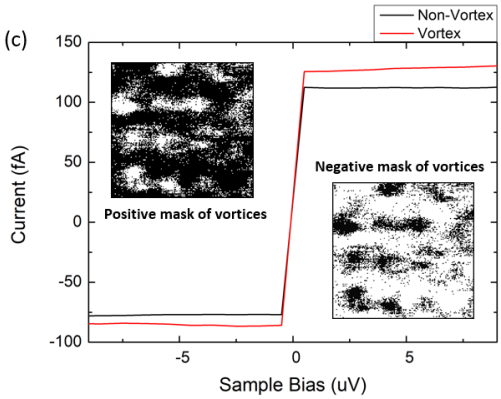

Figure 5.6: Spectroscopic measurement of $Bi_2Sr_2CaCu_2O_8$ from $-10\ \mu eV$ to $10\ \mu eV$ at $25\ mK$ and $13\ T$.

(a) Differential conductance map at zero bias voltage, which shows vortex features (b) Current map at zero bias; a zero bias current map shows no vortex features with a seemingly random noise (c) Comparison of spatially averaged spectra between vortex area with its mask (left inset) and non-vortex area with its mask (right inset)

5.6. Inhomogeneous Bias Offset

Figure 5.7 shows the three possible cases for the charge accumulation on the sample side and their effects on the $I-V$ point spectra. For the neutral net charge on the sample side, the zero bias voltage gives zero tunneling currents. However, if there are negative(positive) net charges on the sample side, the Fermi level is increased. Then there is a current from tip(sample) to sample(tip) since the energy level of tip(sample) side is lower than sample(tip) side.

In other words, if there is no charge inhomogeneity, the ΔV_{offset} distribution will be random (no feature) at zero bias. However, if

there is a charge inhomogeneity, ΔV_{offset} distribution will be correlated to the locations of vortices at zero bias.

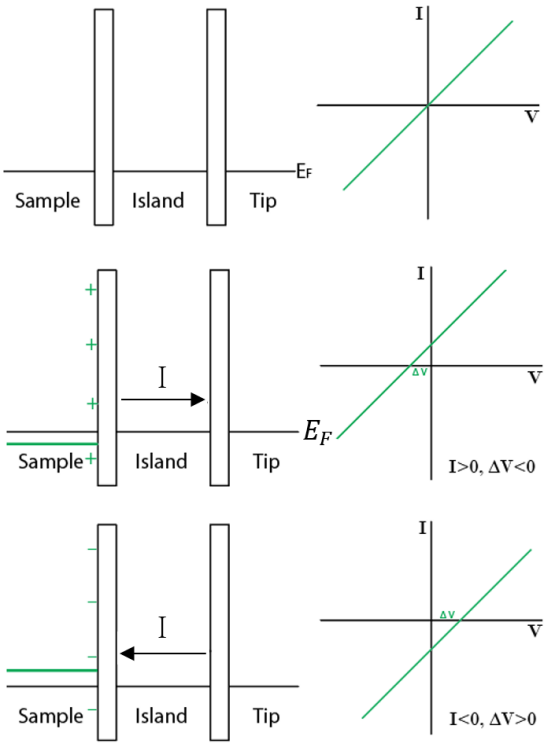

Figure 5.7: Energy diagram of STM measurement with Coulomb blockade tip and their point spectra.

(a) Energy diagram with the neutral charge on the sample side and its point spectrum (b) Fermi level is lowered by positive charges on the sample side, and its corresponding shifted I−V point spectrum (c) Fermi level is raised by negative charges on the sample side, and its corresponding shifted I−V point spectrum

Our Coulomb blockade step features exhibit extremely sharp, well−defined straight I−V lines from which ΔV_{offset} can be determined precisely, which is possible due to the field effect. An extremely

high energy resolution current map with a high spatial resolution near zero bias is needed to visualize a nanoscale spatial distribution of the ΔV_{offset} values.

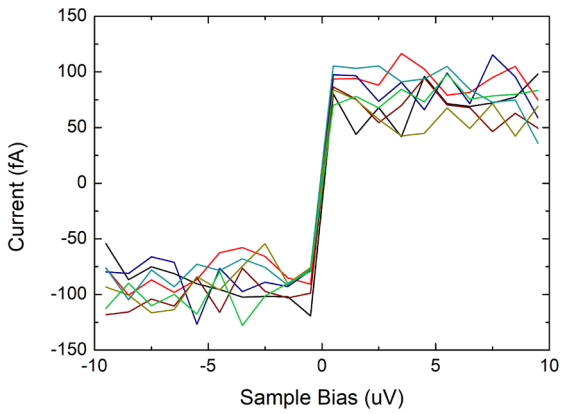

Figure 5.8: I−V point spectra from spectroscopic measurement

5.7. Bias Offset Map

From the previous result, it was shown that the flat region on the point spectra from our spectroscopic measurement is too noisy, so it is not easy to pick up any useful information from them. Instead, we focus on the slope region. The Fig.5.9(a) shows differential conductance image at zero bias in real space $g(r,V)$, which was from the spectroscopic measurement of $\mathrm{Bi_2Sr_2CaCu_2O_{8+x}}$ at $25\,m\mathrm{K}$ and $13\,\mathrm{T}$. It shows clear vortex features, and we can easily find the location of vortices.

In Fig.5.9(a), we measured the bias offset $\Delta\mathrm{V}_{\text{offset}}$, which gives zero current, at each point on the same region $g(r,V)$ of (a). We also checked the cross−correlation between vortex features and the

measured bias offsets. The result shows that there is a strong anti-correlation (negative) between the vortex locations and the measured bias offset ΔV_{offset} (Fig.5.9(c)). According to our data, there is a charge imbalance and ΔV_{offset} is more negative inside the vortices which indicates more positive charge density (lower electron density) (Fig.5.7). Our observation is consistent with the chemical potential imbalance model [35]. The distribution of bias offset is given in Fig.5.9(d), which shows that the magnitude of bias offset is within $1\mu eV$. Fig.5.9(e) shows schematic electron density redistribution around the vortex [40-42]. To determine the vortex charges quantitatively, further research is necessary.

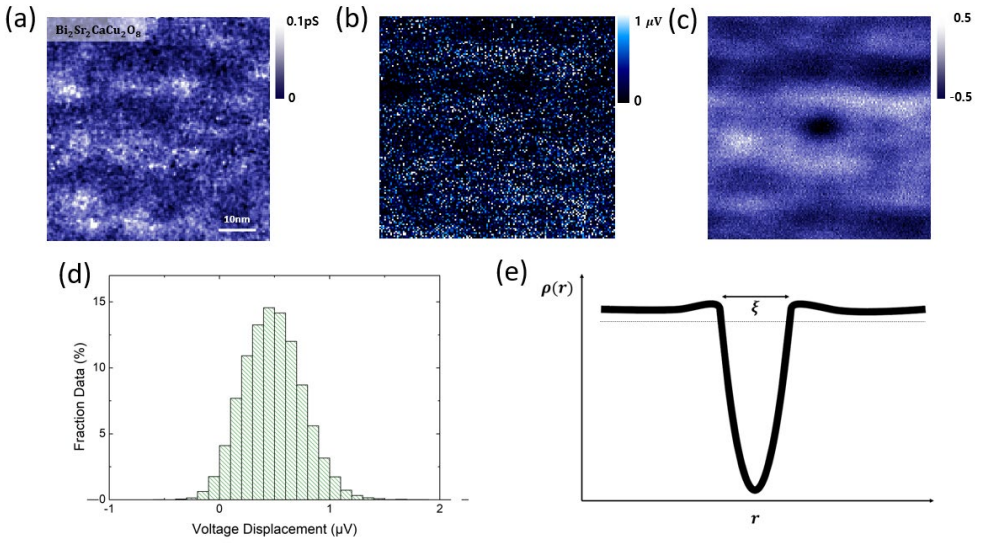

Figure 5.9: Bias-offset Measurement

(a) Differential conductance at zero bias; It shows vortex features (b) ΔV_{offset} map; it shows voltage displacement around vortex area and non-vortex area (c) Cross correlation between differential conductance and ΔV_{offset} map; It shows anti-correlation (d) Distribution of ΔV_{offset} (e) The schematic of electron density redistribution around the vortex

5.8. Summary

We measured a slightly overdoped Bi-2212 sample at $25\,mK$ and $13\,T$ by single electron tunneling microscopy using a Coulomb blockade tip to investigate the vortex charge distribution. According to our result, there is no shift of the Coulomb blockade step itself. Instead, we have utilized the sharpness of the highly nonlinear Coulomb blockade I-V characteristics of our SET tip. We measured the zero bias offset at zero current, and we have fully mapped ΔV_{offset}. For the negative(positive) charge distribution around the sample surface, which is equivalent to the higher(lower) Fermi level on the sample side (Fig.5.7). As a result, the positive(negative) zero bias offset is derived for the negative(positive) charge distribution. Our result shows a negative voltage offset around the vortices compared to the non-vortices, which indicates positive charge accumulation around the vortices, which is the same result with other groups [43,44].

Our result is the first direct visualization of the vortex charges with a spatial resolution, and it is verified that electron density tends to be lower (positive net charge) in vortices than in the non-vortex regions. Further rigorous theoretical analysis might be needed to estimate vortex non-vortex charge imbalance more quantitatively.

Chapter 6.

Conclusion

We have successfully installed the DR-STM and demonstrated its operation by several spectroscopic measurements of $\mathbf{Bi_2Sr_2CaCu_2O_{8+x}}$ as low as $\mathbf{25\ m}\mathbf{K}$ under magnetic field of as high as **13 T**. Using DR-STM with rotational in-situ sample changing stage, various tips were realized: normal metal tip, superconducting tip, SET tip were created in-situ and utilized to characterize the cuprate superconductors.

In this thesis, the vortex charge distribution on the $\mathbf{Bi_2Sr_2CaCu_2O_{8+x}}$ sample has been investigated by DR-STM. We have fully mapped zero bias offset ($\mathbf{\Delta V_{offset}}$) quantitatively around the vortices and non-vortices on the $\mathbf{Bi_2Sr_2CaCu_2O_{8+x}}$ sample. Our result shows the anti-correlation between vortices and zero-bias offset ($\mathbf{\Delta V_{offset}}$). The $\mathbf{\Delta V_{offset}}$ around the vortices is negative, and it represents positive charge accumulation around vortices.

The Coulomb blockade tip is based on the single electron tunneling effect, which is originated from the island on the end of the probe tip. If we can create a Coulomb blockade tip with a smaller capacitance (smaller island) by tip treatment on the gold sample, we can create larger voltage step intervals and we might be able to use single electron tunneling physics to determine vortex charges quantitatively.

In addition, spectroscopic measurements with much higher energy resolution are also required for the quantitative measurement of vortex charge.

Bibliography

[1] G. Binnig, H. Rohrer, Ch. Gerber, and E. Weibel, Surface Studies by Scanning Tunneling Microscopy, Phys. Rev. Lett. **49**, 57–61 (1982)

[2] Ivar Giaever, Energy Gap in Superconductors Measured by Electron Tunneling, Phys. Rev. Lett. **5**, 147–148 (1960)

[3] J. Bardeen, Tunnelling from a Many–Particle Point of View, Phys. Rev. Lett. **6**, 57–59 (1961)

[4] Øystein Fischer, Martin Kugler, Ivan Maggio–Aprile, Christophe Berthod, and Christoph Renner, Scanning tunneling spectroscopy of high–temperature superconductors, Rev. Mod. Phys. **79**, 353–419 (2007)

[5] J. Tersoff and D. R. Hamann, Theory and Application for the Scanning Tunneling Microscope, Phys. Rev. Lett. **50**, 1998–2001 (1983)

[6] S. H. Pan, E. W. Hudson, and J. C. Davis, ^{3}He refrigerator based very low temperature scanning tunneling microscope, Review of Scientific Instruments **70**, 1459–1463 (1999)

[7] J.–J. Kim, S. H. Joo, K. S. Lee, J. H. Yoo, M. S. Park, J. S. Kwak, and Jinho Lee, Improved design for a low temperature scanning tunneling microscope with an in situ tip treatment stage, Review of Scientific Instruments **88**, 043702 (2017)

[8] H. Kamerlingh Onnes, Leiden Commun. **105**, Proc. Roy. Acad. Sci. Amsterdam **11**, 168 (1908)

[9] W.H. Keesom, K. Clusius, Leiden Commun. 219e, Proc. Roy. Acad. Sci. Amsterdam **35**, 307 (1932)

[10] Oliphant, M. L. E. Harteck, P. Rutherford, E, Transmutation Effects Observed with Heavy Hydrogen, Proceedings of the Royal Society A. **144** (853), 692–703 (1934)

[11] J. Franck, Proposal of a Method for the Separation of He^3 from He^4, Phys. Rev. **70**, 561 (1946)

[12] H.A. Fairbank, C.T. Lane, L.T. Aldrich, A.O. Nier, The Concentration of He^3 in the Liquid and Vapor Phases of He^4, Phys. Rev. **71**, 911 (1947)

[13] J. G. Daunt, R. E. Probst, H. L. Johnston, L. T. Aldrich, and Alfred O. Nier, A New Method of Separation of the Isotopes He^3 and He^4, Phys. Rev. **72**, 502 (1947)

[14] J. G. Daunt, R. E. Probst, and H. L. Johnston, The Separation of the Isotopes He^3 and He^4 in the Liquid Phase, J. Chem. Phys. **15**, 759 (1947)

[15] L. Landau, I Ya Pomeranchuk, Motion of extraneous particles in He II'' Dokl. Akad. Nauk SSSR **59**, 669 (1948)

[16] G. K. Walters and W. M. Fairbank, Phase Separation in

He^3—He^4 Solutions, Phys. Rev. **103**, 262–263 (1956)

[17] H. London, G. R. Clarke, and Eric Mendoza, Osmotic Pressure of He^3 in Liquid He^4, with Proposals for a Refrigerator to Work below 1°K, Phys. Rev. **128**, 1992 (1962)

[18] P. Das, R. Bruyn de Ouboter & K. W. Taconis, A Realization of a London–Clarke–Mendoza Type Refrigerator, Low Temperature Physics LT9, 1253–1255 (1965)

[19] J.P. Laheurte, J.R.G. Keyston, Behaviour of He^4 in dilute liquid mixtures of He^4 in He^3, Cryogenics **11**, 485 (1971)

[20] C. Ebner, D.O. Edwards, The low temperature thermodynamic properties of superfluid solutions of ^3He in ^4He, Phys. Rep. **2**, 77 (1971)

[21] L.I. Dana, H. Kamerlingh Onnes, Leiden Commun. 190b, Proc. Roy. Acad. Sci. Amsterdam 29, 1061 (1926)

[22] E.C. Kerr, Density of Liquid He^4, J. Chem. Phys. 26, 511 (1957)

[23] H.K. Onnes, Commun. Leiden, **120b** (1911)

[24] W. Meissner, R. Ochsenfeld, Naturwissenschaften **21**, 787 (1933)

[25] F. London, H. London, Z. Phys. **96**, 359 (1935)

[26] V.L. Ginzburg, L.D. Landau, Zh. Eksperim. i. Teor. Fiz. **20**, 1064 (1950)

[27] J. Bardeen, L.N. Cooper, J.R. Schrieffer, Theory of Superconductivity, Phys. Rev. 108, 1175 (1957)

[28] J.G. Bednorz, K.A. Müller, Possible high T_c superconductivity in the Ba–La–Cu–O system, Z. Phys. B **64**, 189 (1986)

[29] M. K. Wu, J. R. Ashburn, C. J. Torng, P. H. Hor, R. L. Meng, L. Gao, Z. J. Huang, Y. Q. Wang, and C. W. Chu, Superconductivity at 93 K in a new mixed−phase Y−Ba−Cu−O compound system at ambient pressure, Phys. Rev. Lett. **58**, 908 (1987)

[30] Hiroshi Maeda, Yoshiaki Tanaka, Masao Fukutomi, and Toshihisa Asano, A New High−T_c Oxide Superconductor without a Rare Earth Element, Japanese Journal of Applied Physics, **27**, L209 (1988)

[31] Yoichi Kamihara, Hidenori Hiramatsu, Masahiro Hirano, Ryuto Kawamura, Hiroshi Yanagi, Toshio Kamiya, and Hideo Hosono, Iron−Based Layered Superconductor: LaOFeP, J. Am. Chem. Soc. **128**, 31, 10012–10013 (2006)

[32] A. P. Drozdov, M. I. Eremets, I. A. Troyan, V. Ksenofontov & S. I. Shylin, Conventional superconductivity at 203 Kelvin at high pressures in the sulfur hydride system, Nature **525**, 73–76 (2015)

[33] D. V. Averin & K. K. Likharev, Coulomb blockade of single-electron tunneling, and coherent oscillations in small tunnel junctions, Journal of Low Temperature Physics, 62, 345–373 (1986)

[34] D. I. Khomskii and A. Freimuth, Charged Vortices in High Temperature Superconductors, Phys. Rev. Lett. **75**, 1384 (1995)

[35] Gianni Blatter, Mikhail Feigel'man, Vadim Geshkenbein, Anatoli Larkin, and Anne van Otterlo, Electrostatics of Vortices in Type-II Superconductors, Phys. Rev. Lett. **77**, 566 (1996)

[36] Jan Koláček, Pavel Lipavský, and Ernst Helmut Brandt, Charge Profile in Vortices, Phys. Rev. Lett. **86**, 312 (2001)

[37] S. J. Hagen, C. J. Lobb, R. L. Greene, and M. Eddy, Phys. Rev. B **43**, 6246(1991)

[38] A. M. Mounce, S. Oh, S. Mukhopadhyay, W. P. Halperin, A. P. Reyes, P. L. Kuhns, K. Fujita, M. Ishikado & S. Uchida, Charge-induced vortex lattice instability, Nature Physics, **7**, 125–128 (2011)

[39] Ken-ichi Kumagai, Koji Nozaki, and Yuji Matsuda, Charged vortices in high-temperature superconductors probed by NMR, Phys. Rev. B **63**, 144502 (2001)

[40] S. J. Hagen, C. J. Lobb, R. L. Greene, and M. Eddy, Flux-flow

Hall effect in superconducting $Tl_2Ba_2CaCu_2O_8$ films, Phys. Rev. B **43**, 6246 (1991)

[41] Jan Koláček, Pavel Lipavský, and Ernst Helmut Brandt, Charge Profile in Vortices, Phys. Rev. Lett. **86**, 312(2001)

[42] Sudhir Kumar Sahu, Supriya Mandal, Sanat Ghosh, Mandar M. Deshmukh, and Vibhor Singh, Superconducting Vortex-Charge Measurement Using Cavity Electromechanics, Nano Lett. **22**, 4, 1665–1671 (2022)

[43] Tatsuji Nagaoka, Yuji Matsuda, Haruhiko Obara, Akihito Sawa, Takahito Terashima, Iksu Chong, Mikio Takano, and Minoru Suzuki, Hall Anomaly in the Superconducting State of High-Tc Cuprates: Universality in Doping Dependence, Phys. Rev. Lett. **80**, 3594 (1998)

[44] Yan Chen, Z. D. Wang, Jian-Xin Zhu, and C. S. Ting, Vortex Charges in High-Temperature Superconductors, Phys. Rev. Lett. **89**, 217001 (2002)

국문 초록

1986년 고온 초전도체가 발견된 이래 전 세계 수많은 연구자들이 그 원리를 규명하기 위해 수많은 노력을 해왔다. 그 중에서도 특히 터널 주사 현미경은 고온 초전도의 이해를 높이는데 많은 선도적인 역할을 해왔고, 현재도 전 세계 여러 그룹에서 많은 혁신적인 결과들을 발표하고 있다.

일반적으로 터널 주사 현미경을 이용한 초전도 시료의 측정은 액체 헬륨 온도(4.2K)에서 수행되지만, 희석 냉동기를 이용하면 mK 영역의 극저온 환경에서 시료를 측정할 수 있다. 희석 냉동기는 매우 섬세하고 복잡하여 특히 다루기 어렵고 까다로운 장비이며, 동시에 원리적으로 진동이 발생하기 쉬운 장비이다. 반면에 터널 주사 현미경은 진동에 매우 민감한 측정 장비라서, 이 두가지를 결합하는 것은 일반적으로 매우 어려운 작업이다. 우리는 이러한 어려움을 극복하고, 전 세계적으로도 드문 극저온, 초고해상도 터널 주사 현미경을 성공적으로 구현하였다.

이 터널 주사 현미경을 이용하여 극저온, 고자기장 환경에서 전하에 매우 민감한 반응성을 갖는 특별한 Coulomb blockade tip을 만들어 고온 초전도체의 볼텍스 전하 분포에 관한 연구를 수행하였다. 그 결과, 실공간 분해능으로 고온 초전도체의 볼텍스 전하를 직접적으로 처음 관찰하였으며, 또한 고온 초전도체의 볼텍스 영역에서의 전자밀도가 상대적으로 낮아짐을 확인하였다.

감사의 말

먼저 학위 과정동안 지도해주신 이진호 교수님께 감사의 말씀을 드립니다. 희석 냉동기 기반의 터널 주사 현미경을 구현하기까지 수많은 어려움이 있었음에도 물심양면 아낌없는 지원을 하셨으며, 이를 기반으로 숱한 난관을 이겨내고 성공적으로 실험을 마칠 수 있었습니다. 항상 학생들에게 인내심을 갖고 배려하셨으며, 많은 어려움 속에서도 주도적인 역할을 통해 저력 있는 연구자로 성장할 수 있는 가르침을 주셨습니다. 이를 기반으로 박사학위 과정을 무사히 마칠 수 있었습니다.

또한, 어려움이 있을 때 진심으로 같이 고민하고 조언해 주셨던 박수현 박사님께도 감사의 말씀을 전하고 싶습니다. 항상 긍정적인 모습으로 학생들을 대하셨으며, STM의 실질적인 많은 부분을 학생들에게 가르쳐 주시어 무사히 장비를 설치하고 작동시킬 수 있었습니다.

또한, 희석 냉동기를 정상적으로 작동시키기까지 수많은 어려움이 있었음에도 이를 이겨내고 성공적으로 실험을 마칠 수 있었던 것은, 많은 분들의 도움이 있었기에 가능했습니다. 특히, 직접적으로 현장에서 문제해결을 도와주신 것뿐 아니라, 궁금한 점과 어려운 점에 대해 수 없이 많은 질문을 해도, 항상 친절하고 자세하게 가르쳐 주시고, 많은 해결책을 제시해 주신 Fukuzato 엔지니어분께 특별히 감사의 말씀을 전하고 싶습니다.

그리고, 연구실 창립 멤버로서 많은 일을 함께 헤쳐 나왔던 동료들에게 감사의 말을 전합니다. 무엇보다도 장비 문제로 실험이 장기간 지체되었을 때, 실험에 실질적으로 필요한 여러 부분에 도움을 주었던 재준이에게 고마움을 전합니다. 이를 바탕으로 지체된 시간을 상당 부분 절약할 수 있었습니다. 또한 실험실 공사때부터 같이 많이 고생했던 경석이에게

도 고마움을 전하고 싶습니다. 그리고 연구에 어려움이 있을 때, 항상 많은 아이디어를 제시하며 다방면으로 도와준 상현이에게 고마움을 전합니다. 그리고 비록 끝까지 함께하지 못했지만 연구실 초기때부터 같이 고생했던 정훈이 형에게도 고마움을 전하고 싶습니다. 짧은 시간이었지만, 함께 했던 정근이, 성준이, Haibiao, 정수, 세계에게도 고마움을 전합니다.

마지막으로, 항상 저를 믿어 주시는 사랑하는 나의 어머니에게 감사의 말씀을 드립니다.